Inclination Dependence of Kilonova Light Curves from Globally Aspherical Geometries

Siva Darbha[1] and Daniel Kasen[1,2,3]

[1] Department of Physics, University of California, Berkeley, Berkeley, CA 94720, USA; siva.darbha@berkeley.edu
[2] Department of Astronomy and Theoretical Astrophysics Center, University of California, Berkeley, Berkeley, CA 94720, USA
[3] Nuclear Science Division, Lawrence Berkeley National Laboratory, Berkeley, CA 94720, USA

Abstract

The merger of two neutron stars (NSs) or an NS and a black hole (BH) produces a radioactively powered transient known as a kilonova, first observed accompanying the gravitational wave event GW170817. While kilonovae are frequently modeled in spherical symmetry, the dynamical ejecta and disk outflows can be considerably asymmetric. We use Monte Carlo radiative transfer calculations to study the light curves of kilonovae with globally axisymmetric geometries (e.g., an ellipsoid and a torus). We find that the variation in luminosity in these models is most pronounced at early times and decreases until the light curves become isotropic in the late optically thin phase. The light-curve shape and peak time are not significantly modified by the global asymmetry. We show that the projected surface area along the line of sight captures the primary geometric effects, and we use this fact to provide a simple analytic estimate of the direction-dependent light curves of the aspherical ejecta. For the kilonova accompanying GW170817, accounting for asymmetry with an oblate (prolate) ellipsoid of axial ratio 2 (1/2) leads to an $\sim$40% decrease (increase) in the inferred ejecta mass compared to the spherical case. The pole-to-equator orientation effects are expected to be significantly larger (a factor of $\sim$5–10) for the more extreme asymmetries expected for some NS–BH mergers.

1. Introduction

Neutron-rich matter ejected from the merger of two neutrons stars (NSs) or an NS and a black hole (BH) can assemble into heavy elements via rapid neutron capture (the *r*-process; Lattimer & Schramm 1974; Symbalisty & Schramm 1982; Eichler et al. 1989; Freiburghaus et al. 1999). The radioactive decay of the heavy elements produces a thermal transient known as a kilonova (Li & Paczyński 1998; Metzger et al. 2010). The kilonova can be used to infer the properties of the merger, particularly when combined with the gravitational wave (GW) signal; this was shown explicitly in the recent binary NS merger event GW170817/AT 2017gfo (for the GW event, see Abbott et al. 2017a, 2017b; for the kilonova emission, see, e.g., Abbott et al. 2017b; Arcavi et al. 2017; Chornock et al. 2017; Coulter et al. 2017; Cowperthwaite et al. 2017; Drout et al. 2017; Evans et al. 2017; Kasen et al. 2017; Kasliwal et al. 2017; Kilpatrick et al. 2017; Lipunov et al. 2017; McCully et al. 2017; Nicholl et al. 2017; Pian et al. 2017; Shappee et al. 2017; Smartt et al. 2017; Soares-Santos et al. 2017; Tanaka et al. 2017; Tanvir et al. 2017; Villar et al. 2017).

The NS–NS mergers may eject mass via three general mechanisms (Metzger 2017): tidal tails that are stripped from the tidally disrupted stars during inspiral, a shocked outflow that is expelled from the collision interface, and a disk wind emitted by the accretion disk formed after the merger. The first two mechanisms are referred to as the dynamical ejecta of the merger. In addition to these three processes, NS–NS mergers may produce outflows driven by more particular or speculative mechanisms (Fujibayashi et al. 2018; Metzger et al. 2018; Radice et al. 2018a; Nedora et al. 2019).

The composition of an ejecta is determined by the electron fraction $Y_e = n_p/(n_n + n_p)$, where n_p and n_n are the number densities of protons/electrons and neutrons, respectively. Neutron-rich ejecta ($Y_e \lesssim 0.25$) can synthesize *r*-process material past the second *r*-process peak at $A \sim 130$, including

the lanthanide species known to have very high opacities (Kasen et al. 2013). The emission when lanthanides are present has a redder spectrum and a later and broader peak (Barnes & Kasen 2013; Kasen et al. 2013).

Simulations of NS–NS mergers indicate that their ejecta are likely aspherical. The tidal tails lie primarily in the equatorial plane and have low Y_e ($\lesssim$0.25), and the shocked material lies primarily in a conical polar region and has a higher Y_e due to neutrino and weak interactions (for early work on the tidal tails with Newtonian codes, see Rosswog et al. 1999, 2000; for more recent work on the tidal tails and collision ejecta with relativistic codes, see, e.g., Bauswein et al. 2013; Hotokezaka et al. 2013; Radice et al. 2016, 2018b; Dietrich et al. 2017). The wind from the postmerger disk is fairly spherical, though mildly prolate, and likely comprised of a broad distribution of Y_e (Perego et al. 2014; Siegel & Metzger 2017, 2018; Fujibayashi et al. 2018; Radice et al. 2018b; Fernández et al. 2019). The properties of the NSs and the binary system will influence the geometry and mass of each of these components. Mergers with more asymmetric mass ratios produce more massive tidal ejecta, and mergers with lower-radius NSs produce more massive shocked ejecta. More massive disk winds are produced by mergers with more asymmetric mass ratios or longer-lived NS remnants. The ejecta from NS–BH mergers is similar but with two main differences: there is a single large tidal tail from the disruption of the NS only, and there is likely no collision interface ejecta, since the BH does not have a material surface (e.g., Foucart et al. 2013, 2019; Kyutoku et al. 2013, 2015; Kawaguchi et al. 2015; Kiuchi et al. 2015).

The initial radiative transfer models of kilonovae assumed spherical symmetry (Metzger et al. 2010; Barnes & Kasen 2013; Kasen et al. 2013). These were used to fit the light curves and spectra of the event AT 2017gfo and infer its basic properties (e.g., Chornock et al. 2017; Cowperthwaite et al. 2017; Kasen et al. 2017; Kilpatrick et al. 2017; Nicholl et al. 2017; Tanaka et al. 2017; Villar et al. 2017). Following

this, several studies have examined aspherical kilonova ejecta using both radiative transfer simulations and semianalytic models. Roberts et al. (2011) carried out 3D radiation transport simulations and found a factor of ∼3 variation in the brightness with viewing angle. Subsequent radiation transport simulations that aimed to replicate the realistic, heterogeneous, multi-component ejecta structure have found similar results (Kasen et al. 2015, 2017; Kawaguchi et al. 2018, 2020; Wollaeger et al. 2018; Bulla 2019). Grossman et al. (2014; and subsequently, Perego et al. 2014; Martin et al. 2015) used a semianalytic "diffusive model" to postprocess the ejecta from merger simulations and found a factor of ∼2 variation in the brightness with viewing angle. Barbieri et al. (2019) recently developed an autonomous semianalytic model for multi-messenger parameter estimation and derived a projection factor that yields a factor of ∼2–3 variation.

A robust understanding of the dependence of kilonova light curves on geometry and inclination is needed to more accurately estimate the properties of kilonova ejecta (e.g., mass, kinetic energy, opacities). In addition, a constraint on the inclination of the NS–NS merger from the kilonova would partly break the distance–inclination degeneracy in the GW data and reduce the number of detections needed for an accurate Hubble constant measurement using joint kilonova/ GW observations (Abbott et al. 2017c; Feeney et al. 2019). We note, though, that the inclination can also be measured by other means (Mooley et al. 2018; Hotokezaka et al. 2019), and the Hubble constant can be measured with the GW or kilonova data alone (Coughlin et al. 2020; Fishbach et al. 2019).

In this paper, we study the time-domain signatures from aspherical kilonovae produced by NS–NS and BH–NS mergers. In particular, we consider simple geometric models that describe the global behavior of kilonova ejecta to build intuition into how viewing angle effects depend on geometry. We focus on an ellipsoid and a ring torus and extend our analysis to a conical section embedded in a sphere. We characterize the systematic uncertainties involved in using a spherical or aspherical model and quantify the uncertainties as a function of sphericity. We find that the scale of the light-curve variation with viewing angle is primarily determined by the projected surface area, and the light curves converge with time as they become more isotropic.

In Section 2, we outline the parameters and geometries of our ejecta models. In Section 3, we present our results and provide a simple, semianalytic prescription to estimate the direction-dependent light curve of the aspherical ejecta from the light curve of the equivalent spherical ejecta. In Section 4, we discuss the range and limitations of our results and apply them to a general conical geometry and to AT 2017gfo. In Appendix A, we provide equations for the parallel projected areas of our geometries. In Appendix B, we present the fitting parameters, discuss the limitations of the semianalytic prescription of Section 3, and provide more involved parameterizations.

2. Methods

2.1. General Properties

We study the emission from a homologously expanding ejecta using the time-dependent Monte Carlo radiative transfer code SEDONA (Kasen et al. 2006). We study an ejecta with mass M and kinetic energy $E_k = M v_{ch}^2/2$, where $v_{ch} = \beta_{ch} c$ is

the characteristic velocity and c is the speed of light. We use a one-component, constant gray opacity κ to parameterize the strength of the interaction between the thermal photons and matter.

The light-curve evolution is determined by two timescales. The first is the effective diffusion timescale $t_d = (M\kappa/v_{ch} c)^{1/2}$, which characterizes the time at which photons escape the ejecta faster than the ejecta can expand. We take this as our definition of t_d but note that other definitions exist that contain additional numerical factors (Arnett 1982). We use this to define the dimensionless time $\tau = t/t_d$, where t is the physical time. The second is the thermalization timescale t_e, which characterizes the time at which the absorption of radioactive decay products begins to become inefficient. This can be written in terms of the dimensionless parameter $\tau_e = t_e/t_d$. For neutron-rich ejecta, the radioactive power from the r-process alone can be approximated by a power law (Metzger et al. 2010; Lippuner & Roberts 2015; Hotokezaka et al. 2017) and thus does not itself have an intrinsic timescale. We note that ejecta with $Y_e \gtrsim 0.35$ can exhibit a different time dependence (Wanajo et al. 2014).

The light curves are powered by the radioactive decay of neutron-rich elements synthesized by the r-process (Metzger et al. 2010). The fraction of the radioactive power that will thermalize and contribute to the electromagnetic emission is determined by its distribution in the different decay channels (beta, alpha, and fission) and their thermalization efficiencies (Metzger et al. 2010; Barnes et al. 2016), though the total contribution can be reduced to a simple approximate prescription (Kasen & Barnes 2019). We adopt the latter, yielding the specific heating rate

$$q(\tau; \tau_e) = q_0 t_{d,day}^{\sigma_1} \tau^{\sigma_1} \left(1 + \frac{\tau}{\tau_e}\right)^{\sigma_2}, \qquad (1)$$

where τ_e is the thermalization timescale, $t_{d,day}$ is the diffusion time in days, and we take $q_0 = 10^{10}$ erg s^{-1} g^{-1}, $\sigma_1 = -1.3$, and $\sigma_2 = -1.2$. The term τ_1^σ gives the time dependence of the radioactive power from an ensemble of r-process nuclei (Metzger et al. 2010; Lippuner & Roberts 2015; Hotokezaka et al. 2017), and the term in parentheses is the thermalization efficiency (Kasen & Barnes 2019). We take $\tau_e = 10$ for our canonical example but also examine the effects of different values. The total heating rate is then $Q = Mq$.

Given the above specific heating rate, we define the dimensionless luminosity $\Lambda = L/L_n$, where L is the physical luminosity and $L_n = Mq_0 t_{d,day}^{\sigma_1}$ is the scale factor. If all parts of the outflow are in the diffusive regime, then ejecta profiles with the same τ_e would be degenerate and exhibit the same dimensionless light curves $\Lambda(\tau)$; i.e., the light-curve shape and anisotropy will not depend on the individual values of M, κ, β_{ch}, and q_0 but rather only on the combinations $t_d = (M\kappa/\beta_{ch} c^2)^{1/2}$ and $L_n = Mq_0 t_{d,day}^{\sigma_1}$ (as well as the variables τ_e, σ_1, etc.). In practice, this scaling breaks down for outflows with a sufficiently high β_{ch} or low M, for which the outer ejecta layers are of low density and become optically thin. However, for a given τ_e, we find that outflows with $\beta_{ch} \lesssim 0.1$ generally remain in the diffusive regime.

With the above framework and qualifications, we run our simulations with the fiducial ejecta parameters $M = 10^{-2} M_\odot$, $\beta_{ch} = 0.1$, and $\kappa = 1$ cm^2 g^{-1}. We start our simulations at the initial time $\tau_0 = 0.01$ and nondimensionalize our results.

(a) Ellipsoid   (b) Torus   (c) Conical Section
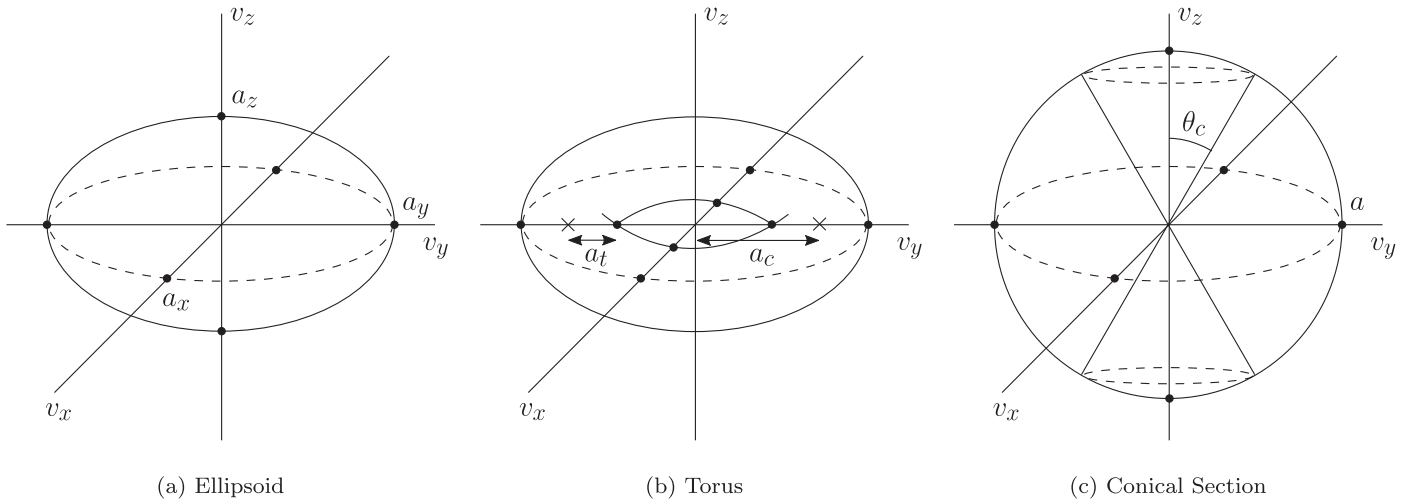
Figure 1. Three ejecta geometries studied in this paper. The black dots show the points where the axes intersect the surfaces. (a) Ellipsoid. The semimajor axes are (a_x, a_y, a_z), and we study the axisymmetric case $a_x = a_y$ (spheroid) with axial ratios $R = a_x/a_z$ (oblate here, $R > 1$). (b) Torus. The spine radius is a_c and the tube radius is a_t, and we study radius ratios $K = a_c/a_t > 1$ (ring torus). The crosses mark the points where the torus spine (i.e., the center of the tube) intersects the v_y-axis. (c) Conical section embedded in a sphere. The sphere has a radius a, and the conical section has a half-opening angle θ_c.

2.2. Geometries

We study several idealized axisymmetric geometries that can represent the ejecta from a kilonova as described in Section 1. We summarize these geometries in Figure 1. We primarily study an ellipsoid and a ring torus and extend our analysis to a conical section embedded in a sphere.

These geometries are robust and versatile and can replicate the shape of the different ejecta components described in Section 1. An ellipsoid is one of the simplest geometries that has dipolar asymmetry and thus serves as a generic model for deviations from sphericity. A modestly prolate ellipsoid with an axial ratio R (defined in Section 2.2.1) near unity can serve as a model for the disk wind, which magnetohydrodynamics (MHD) simulations have shown can have a global distortion (Fernández et al. 2019), with the amount of mass ejection varying by ∼2 from pole to equator. An oblate ellipsoid with $R \gtrsim 2$ can serve as a model for the tidal tail, and a prolate ellipsoid with $R \lesssim 1/2$ can serve as a model for the collision interface ejecta. A torus with a radius ratio K (defined in Section 2.2.2) near unity can serve as a model for the wind in the aftermath of jet puncture, and one with $K \gtrsim 2$ can also serve as a model for the tidal tail. A conical section embedded in a sphere can serve as a model for the low-opacity polar ejecta from the collision enshrouded by both the high-opacity equatorial ejecta from the tidal tail and the postmerger wind.

Since the geometries we study are axisymmetric, we parameterize the viewing angle with $\mu = \cos\theta$, where θ is the polar angle measured from the z-axis. We record the emission in 20 uniformly spaced bins in $\mu \in [-1, 1]$. In Appendix A, we calculate the parallel projected areas as a function of μ for each of these geometries, which are useful for understanding the light curves.

2.2.1. Ellipsoid

We study an ellipsoid with velocity coordinates (v_x, v_y, v_z) and velocity space semimajor axes (a_x, a_y, a_z), where $a_x = a_y$ (axisymmetric, spheroid). We define the axial ratio $R = a_x/a_z$ and examine several values in the range $R \in [1/4, 6]$. We

define the dimensionless velocity coordinate

$$s = \left[\left(\frac{v_x}{a_x}\right)^2 + \left(\frac{v_y}{a_y}\right)^2 + \left(\frac{v_z}{a_z}\right)^2 \right]^{1/2}, \qquad (2)$$

where $0 \leqslant s \leqslant 1$. A surface of constant s is the surface of an ellipsoid with its center at the origin and semimajor axes (sa_x, sa_x, sa_z); $s = 1$ corresponds to the outer surface of the ejecta.

We adopt a density profile of the form $\rho = \rho(s, \tau)$, in which surfaces of constant density correspond to surfaces of constant s. We study two types: (1) a constant density profile with a sharp cutoff at the surface and (2) a broken power-law density profile. The constant profile is given by $\rho_c(s, \tau) = \rho_{c0}(\tau_0)(\tau_0/\tau)^3$. The broken power-law profile has been successfully used to model kilonovae and more general transients (Chevalier & Soker 1989; Barnes & Kasen 2013; Kasen et al. 2017) and is given by

$$\rho_b(s, \tau) = \rho_{b0}(\tau_0)\left(\frac{\tau_0}{\tau}\right)^3 \begin{cases} \left(\frac{s}{s_b}\right)^{\delta_1}, & s < s_b \\ \left(\frac{s}{s_b}\right)^{\delta_2}, & s_b \leqslant s \leqslant 1. \end{cases} \qquad (3)$$

Here s_b is the location of the break in the power law, and δ_1 and δ_2 are the exponents in the broken power law that satisfy $0 > \delta_1 > -3$ and $\delta_1 > \delta_2$ to have a declining profile that decreases more precipitously after s_b and has finite M and E_k. We take $s_b = 0.5$, $\delta_1 = -1$, and $\delta_2 = -10$. We examine these two types of profiles in order to identify the trends in our results that are robust to changes in the form or parameters of the density profile. We use the values of M, β_{ch}, and τ_0 given in Section 2.1 and choose a value for R, and this sets the parameters a_x, a_z, and either $\rho_{c0}(\tau_0)$ or $\rho_{b0}(\tau_0)$.

2.2.2. Torus

We study a torus with velocity coordinates (v_x, v_y, v_z), velocity space spine radius a_c, and tube radius a_t, where $a_c \geqslant a_t$ (ring torus). We define the radius ratio $K = a_c/a_t \geqslant 1$ and

(a) **Scaled by** $L_n = Mq_0 t_{d,\text{day}}^{\sigma_1}$

(b) **Scaled by** $L_{\text{av}}(\tau; R)$
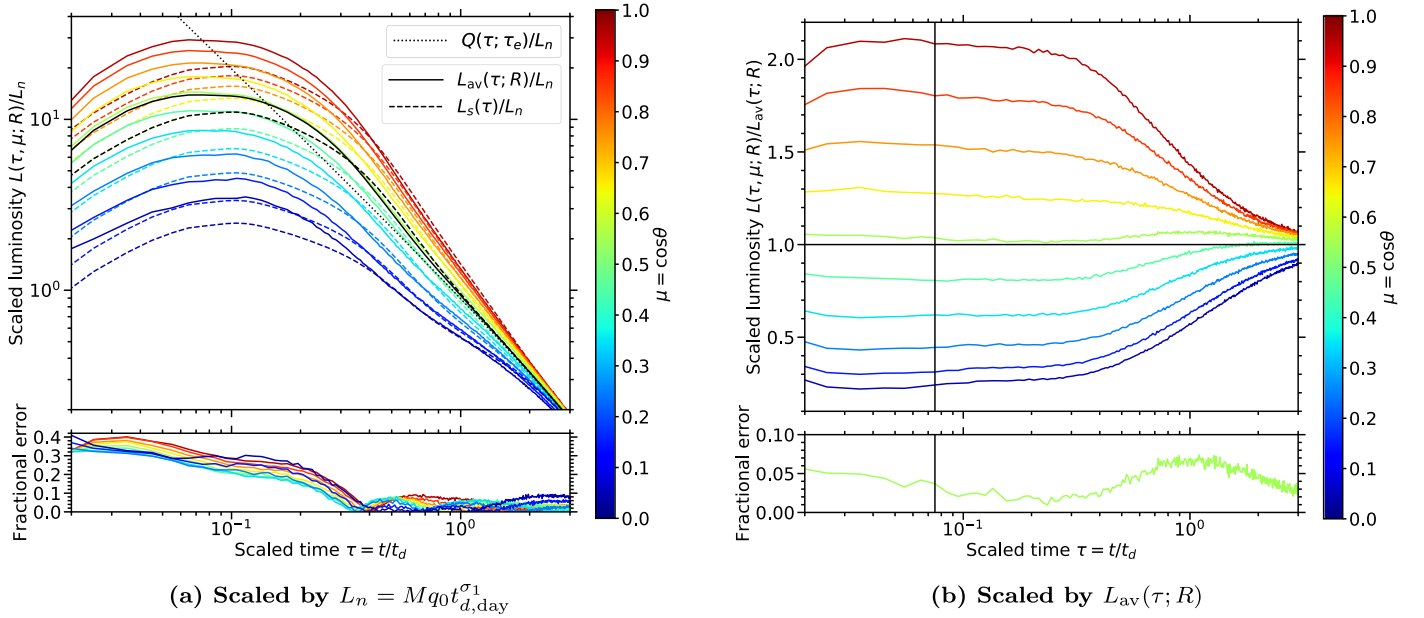
Figure 2. The isotropic-equivalent bolometric light curves $L(\tau, \mu; R)$ for an ellipsoid outflow with a broken power-law density profile and axial ratio $R = 4$ at different viewing angles $\mu = \cos\theta$. The time t has been scaled by the diffusion time t_d as $\tau = t/t_d$, and the thermalization time is $\tau_e = 10$. (a) The isotropic-equivalent luminosity has been scaled by the factor $L_n = Mq_0 t_{d,\text{day}}^{\sigma_1}$ (Section 2.1). The solid black curve shows the angle-averaged luminosity, the dashed black curve shows the luminosity of the equivalent spherical ejecta ($R = 1$ with the same τ_e), and the dotted black curve shows the total heating rate. The dashed colored curves show the curve fits using the functions in Equations (9) and (10). The bottom panel shows the error of the fits. (b) The isotropic-equivalent luminosity has been scaled by the angle-averaged luminosity $L_{\text{av}}(\tau; R)$. The solid black horizontal line shows the angle-averaged luminosity, and the solid black vertical line shows its time to peak. The bottom panel shows the error of $L(\tau, \mu_{\text{ref}}; R)$ from $L_{\text{av}}(\tau; R)$ for $\mu_{\text{ref}} = 0.55$.

examine several values in the range $K \in [1, 5]$. We define the dimensionless velocity coordinate

$$s = \frac{[((v_x^2 + v_y^2)^{1/2} - a_c)^2 + v_z^2]^{1/2}}{a_t}, \quad (4)$$

where $0 \leqslant s \leqslant 1$. A surface of constant s is the surface of a torus with spine radius a_c and tube radius sa_t; $s = 1$ corresponds to the outer surface of the ejecta.

We adopt the same types of density profile as in Section 2.2.1, though with two modifications: the variable s has the present definition, and the exponents satisfy $0 > \delta_1 > -2$ and $\delta_1 > \delta_2$. We take the same values for s_b, δ_1, and δ_2. We use the values of M, β_{ch}, and τ_0 given in Section 2.1 and choose a value for K, and this sets the parameters a_c, a_t, and either $\rho_{c0}(\tau_0)$ or $\rho_{b0}(\tau_0)$.

3. Results

The features of kilonova light curves are determined by the properties of the underlying ejecta, and robust models are needed to extract the ejecta parameters from the observed light curves. In this section, we quantify the geometric effects that exist in aspherical ejecta and present a simple and intuitive method to roughly estimate the anisotropic light curves of aspherical kilonovae given the light curve of the equivalent spherical model (with the same M, E_k, and τ_e).

We first study an ellipsoid as a generic model for dipolar deviations from sphericity. The bolometric light curves from this geometry serve as a surrogate for the frequency-integrated (e.g., blue or red) unobstructed light curves of the different ejecta components after reintroducing the appropriate scales. We focus on a broken power-law density profile and highlight the differences in the constant density case. We then examine a torus and describe the geometry-specific differences compared to the ellipsoid. Appendix B presents the values of various

fitting parameters and approximations used in our prescriptions for both geometries and density profiles. The numerical models are also available if accurate light curves are needed.
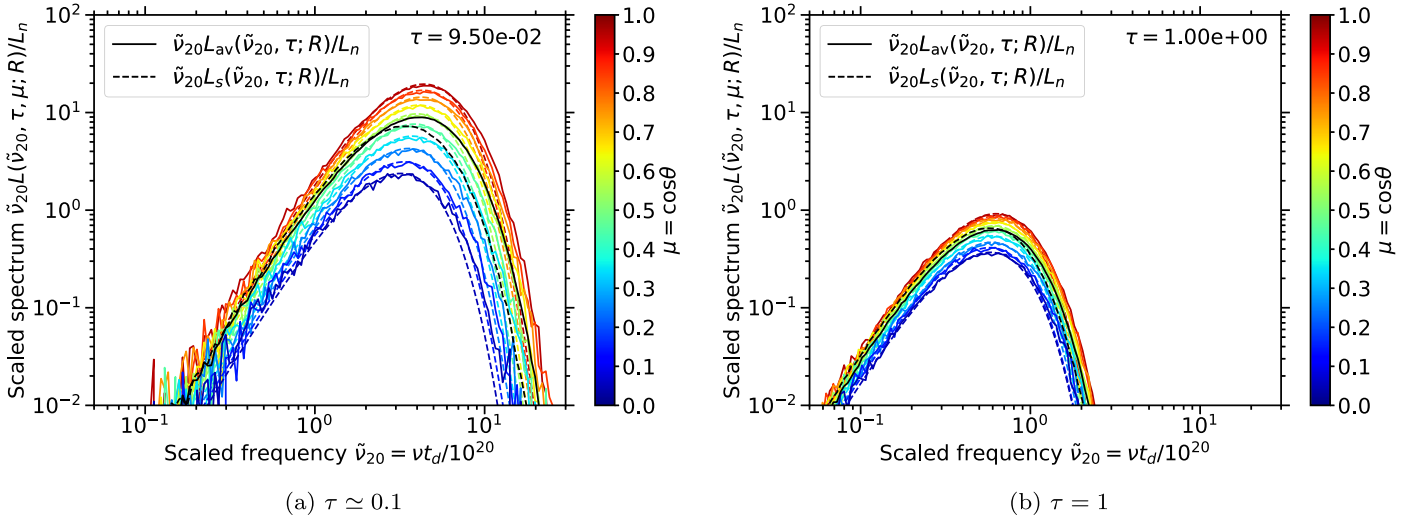
3.1. Ellipsoid

Figure 2 shows the isotropic-equivalent light curves $L(\tau, \mu; R)$ for the ellipsoidal kilonova with a broken power-law density profile and an axial ratio $R = 4$. The viewing angle is defined by $\mu = \cos\theta$ (where θ is the polar angle measured from the z-axis), and each value of μ has equal probability of being observed. The light curves are invariant under the transformation $\mu \to -\mu$ due to reflection symmetry about $z = 0$, so the figure shows only the viewing angles $\mu > 0$.

The light curves of the ellipsoidal model are brightest along the pole ($\theta = 0$, or $\mu = 1$) and dimmest along the equator ($\theta = \pi/2$, or $\mu = 0$). The total variation in the luminosity at peak is a factor of ~ 9. The time to peak $\tau_p(\mu; R) \sim 0.1$, though, remains largely unchanged with viewing angle. The viewing angle dependence is most pronounced at early times but decreases over time until the light curves become mostly isotropic by $\tau \sim 5$ and converge to the total heating rate $Q(\tau; \tau_e)$. This is because at late times, the ejecta becomes fully optically thin, so that all parts of the ejecta radiate equally in all directions (apart from small relativistic corrections).

Figure 2 also shows the angle-averaged light curve $L_{\text{av}}(\tau; R)$ of the ellipsoidal model and the isotropic-equivalent light curves normalized to this. The light curve of an intermediate viewing angle $\mu_{\text{ref}} \approx 0.55$ ($\theta_{\text{ref}} \approx 57°$) roughly equals the angle-averaged light curve, $L(\tau, \mu_{\text{ref}}; R) \simeq L_{\text{av}}(\tau; R)$, with an error $\epsilon < 0.1$. The polar light curves are brighter than these, and the equatorial ones are dimmer. The angle-averaged light curve is comparable to the light curve $L_s(\tau)$ of the equivalent spherical model ($R = 1$ with the same τ_e), $L_{\text{av}}(\tau; R) \simeq L_s(\tau)$, with an error $\epsilon < 0.5$ (Figure B3).

Figure 3. Spectra for an ellipsoid outflow with a broken power-law density profile and axial ratio $R = 4$ at different viewing angles and times. The time t has been scaled by the diffusion time t_d as $\tau = t/t_d$, the frequency ν has been scaled as $\tilde{\nu}_{20} = \nu t_d/10^{20}$, and the luminosity $L(\tilde{\nu}_{20}, \tau, \mu; R)$ has been scaled by $\tilde{\nu}_{20}$ and $L_n = M q_0 t_{d,\text{day}}^{\sigma_1}$ (Section 2.1). The spectra are shown at times (a) $\tau \simeq 0.1$ and (b) $\tau = 1$. The solid black curves show the angle-averaged spectra, and the dashed black curves show the spectra of the equivalent spherical ejecta. The dashed colored curves show the curve fits to an effective blackbody (Equation (7)).

The basic viewing angle dependence of the light curves can be understood by considering the parallel projected surface area of the ejecta at different inclinations. If we consider a simple approximation in which an ellipsoidal photospheric shell emits blackbody radiation at a fixed temperature T_{bb}, then the luminosity would be proportional to the projected area, which is found to be (Appendix A.1)

$$A_{\text{proj}}(\mu; R) = \pi R a_z^2 [(R^2 - 1)\mu^2 + 1]^{1/2}. \qquad (5)$$

For an oblate ellipsoid, the projected area is a maximum along the pole and decreases monotonically to a minimum at the equator. The pole-to-equator projected area ratio is

$$\frac{A_{\text{proj}}(\mu = 1; R)}{A_{\text{proj}}(\mu = 0; R)} = R, \qquad (6)$$

and this gives a rough scale for the luminosity variation of the light curve from pole to equator.

In reality, the kilonova ejecta is not described by a constant temperature ellipsoidal photosphere. Rather, the photosphere recedes with time, and there will be emission from a surface of nonconstant temperature plus emission from the optically thin volume outside the photosphere. The different viewing angles will have different effective diffusion times and effective photospheric parameters. Nevertheless, we show below that the projected area appears to capture the primary geometric effects on the light curve.

Figure 3 shows the spectra as a function of viewing angle at two different times for $R = 4$. The spectra for different μ are well described by an effective blackbody,

$$L(\nu, \tau, \mu; R) = 4\pi R_{\text{surf}}^2(\tau) B(\nu, T_{\text{eff}}(\tau)), \qquad (7)$$

where ν is the photon frequency and B is the blackbody spectrum,

$$B(\nu, T_{\text{eff}}) = \frac{2h\nu^3/c^2}{e^{h\nu/kT_{\text{eff}}} - 1}, \qquad (8)$$

with effective temperature T_{eff} and effective areal radius R_{surf}. The blackbody form arises because we used a constant gray opacity (Section 2.1). The effective temperatures and radii increase with projected surface area: they are larger for μ toward the poles and smaller for μ toward the equator. The temperatures decrease and the radii increase with time until $\tau \sim 2$; the temperatures then converge to one constant value, and the radii decrease exponentially with time while retaining their dependence on μ. The viewing angle variation of the spectra thus decreases with time, as expected from the light curves.

Figure 4 shows the variation of the luminosity ratio $L(\tau, \mu; R)/L(\tau, \mu_{\text{ref}}; R)$ with viewing angle at different times for $R = 4$. At the time $\tau \simeq 0.65$ (not shown in the figure), the angular dependence is remarkably well fit by the ratio of projected surface areas $A_{\text{proj}}(\mu; R)/A_{\text{proj}}(\mu_{\text{ref}}; R)$ (Equation (5)). At other times, the viewing angle dependence has the same shape (Figure A1) but with a different scale. This suggests that we can roughly describe the basic behavior of the light curve with a simple time-dependent function of the projected area (Equation (5)), such as

$$\frac{L(\tau, \mu; R)}{L(\tau, \mu_{\text{ref}}; R)} \simeq 1 + k(\tau; R)\left(\frac{A_{\text{proj}}(\mu; R)}{A_{\text{proj}}(\mu_{\text{ref}}; R)} - 1\right), \qquad (9)$$

where $k(\tau; R)$ is a dimensionless fitting parameter that describes the scale of the viewing angle variation as a function of time. The dashed lines in Figure 4 show the fits to $L(\tau, \mu; R)/L(\tau, \mu_{\text{ref}}; R)$ using this function.

The fitting parameter $k(\tau; R)$ rises with time to a peak around $\tau \sim 0.3$ and then decays to zero roughly exponentially (Figure B1). We can see its effect in Figure 2, which shows the ratio $L(\tau, \mu; R)/L_{\text{av}}(\tau; R)$ as a function of time for $R = 4$. The curves show that the orientation effects are largest at early times, when the ejecta is optically thick, and converge at late times, when the ejecta becomes optically thin and the emission becomes isotropic (apart from Doppler shift effects, which are small for the values of β_{ch} of interest). The effects fall off roughly exponentially with time.
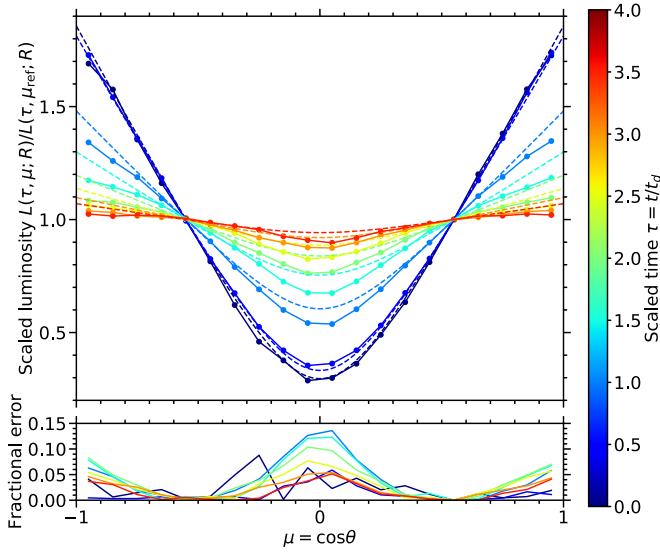
Figure 4. Isotropic-equivalent bolometric luminosities for an ellipsoid outflow with a broken power-law density profile and axial ratio $R = 4$ as a function of viewing angle $\mu = \cos\theta$ and at different times. The time t has been scaled by the diffusion time t_d as $\tau = t/t_d$ (Section 2.1), and the isotropic-equivalent luminosity $L(\tau, \mu; R)$ has been scaled by that in the reference direction $\mu_{ref} = 0.55$, since in this direction, the luminosity roughly equals the angle-averaged luminosity. The thermalization time is $\tau_e = 10$. The points and solid colored curves show the luminosities at different values of $\tau < 4$. The dashed colored curves show the fits to the function in Equation (9). The bottom panel shows the error of the fits.
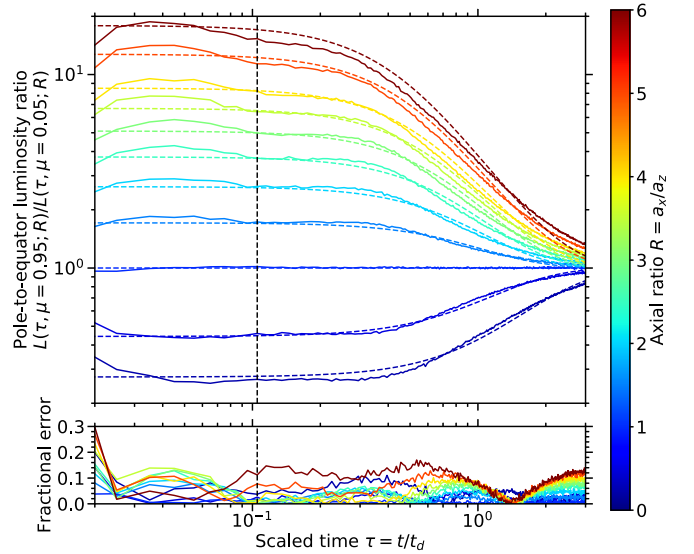
A more detailed inspection suggests that we can approximate $k(\tau; R)$ with the analytic expression

$$k(\tau; R) \simeq k_0(R) \frac{2 + \tau/\tau_b(R)}{1 + e^{\tau/\tau_b(R)}} \qquad (10)$$

with the fitting parameters $k_0(R)$ and $\tau_b(R)$, where $k_0(R)$ sets the value at $\tau = 0$ and $\tau_b(R)$ is an estimate of the timescale for the anisotropy to decay. At early times $\tau \ll \tau_b(R)$, the expression becomes $k(\tau; R) \sim k_0(R)$ with $\partial_\tau k = 0$. At late times $\tau \gg \tau_b(R)$, it becomes $k(\tau; R) \sim \tau e^{-\tau/\tau_b(R)}$, which is close to the observed exponential falloff. Using this expression for $R = 4$, we find the values $k_0 = 1.4$ and $\tau_b = 0.59$ and the fit residual $|\delta| < 0.1$ (Figure B1).

We can thus obtain a rough projection factor from $L_s(\tau)$ to $L(\tau, \mu; R)$ by using Equation (9), with the replacement $L(\tau, \mu_{ref}; R) \to L_s(\tau)$, and Equation (10), with the values given for k_0 and τ_b. Figure 2 shows the semianalytic light curves for $R = 4$ obtained by applying this projection factor, along with their errors. The projected light curves are not impeccable; they typically have lower peaks and converge more quickly to the heating rate at late times. However, they are accurate to within an error of $\epsilon \lesssim 0.4$ before peak and $\epsilon \lesssim 0.3$ after peak and thus roughly capture the temporal evolution of the emission and the correct scale of the variation.

The projection factor obtained from this approach provides a workable estimate of the viewing angle dependence, though it has limitations and should not be used cavalierly. First, the fitting parameter $k(\tau; R)$ rises to a peak and decays, and is bounded above because Equation (9) must be positive; in contrast, the analytic approximation in Equation (10) starts at a peak with zero slope and decreases monotonically with increasing τ. Second, the angle-averaged light curves $L_{av}(\tau; R)$ are not quite equal to the equivalent spherical light curves

$L_s(\tau)$, and the divergence between the two is more pronounced for larger axial ratios. Appendix B quantifies the scale of these effects and provides more accurate but more involved parameterizations.

The features presented above for $R = 4$ generalize over our range of $R \in [0.25, 6]$. Ejecta with higher R have a larger spread in brightness since the projected area changes more from pole to equator (Equation (6)). The time to peak $\tau_p(\mu; R)$ is largely insensitive to R in addition to μ and falls within $0.05 \leqslant \tau_p(\mu; R) \leqslant 0.12$. The various fits and approximations are more accurate for R closer to unity and grow less accurate with increasing asphericity. The relation $L(\tau, \mu_{ref}; R) \simeq L_{av}(\tau; R)$ for the reference value $\mu_{ref} = 0.55$ has errors $\epsilon \lesssim 0.1$. The relation $L_{av}(\tau; R) \simeq L_s(\tau)$ has an error $\epsilon < 0.1$ for $0.25 \leqslant R \leqslant 2$, rising to $\epsilon < 0.9$ for $R = 6$ (Figure B3). For different R, the fitting parameter $k(\tau; R)$ has a similar time evolution, and the analytic approximation for $k(\tau; R)$ remains robust (Figure B1). The semianalytic light curves have errors $\epsilon < 0.2$ for $0.25 \leqslant R \leqslant 2$, rising to $\epsilon < 0.6$ for $R = 6$, which are comparable to those from uncertainties in the opacity (Barnes & Kasen 2013) and heating rate (Metzger et al. 2010; Korobkin et al. 2012; Lippuner & Roberts 2015). More simply, we find that the constant values $k_0(R) \simeq 1.2$ and $\tau_b(R) \simeq 0.7$ produce semianalytic light curves within these error bounds.

We summarize the inclination dependence for different R with the pole-to-equator luminosity ratio, shown in Figure 5. The curves inherit the behavior described in Figures 2 and 4 and the related text. In particular, at early times, the luminosity ratio is larger than the corresponding projected area ratio ($\sim R$; Equation (6)), and at late times, it approaches unity as the emission becomes isotropic. The dashed colored curves show fits using the analytic approximations in Equations (9) and (10) with the fitting parameters $k_0(R)$ and $\tau_b(R)$ in Figure B1. The fits are accurate within errors $\epsilon < 0.3$ during the rise phase $\tau \lesssim \tau_p(\mu; R) \sim 0.1$ and $\epsilon < 0.2$ after this.
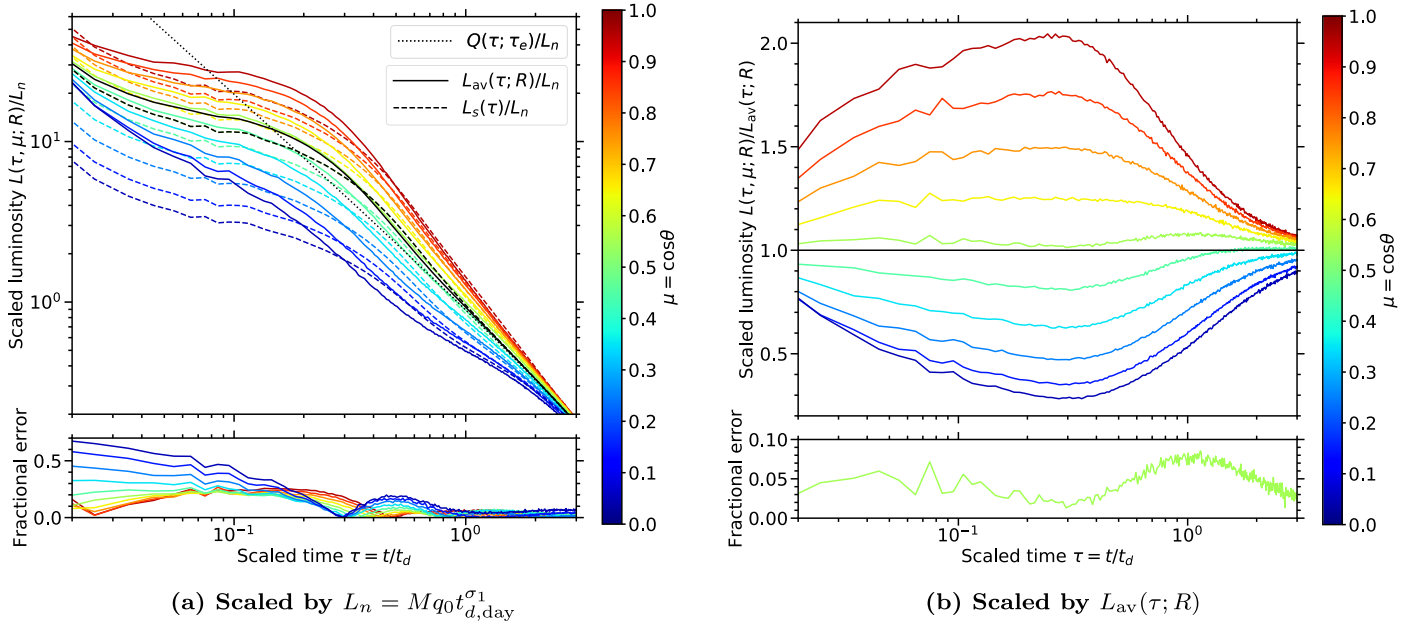

Figure 5. Pole-to-equator light-curve ratio for an ellipsoid outflow with a broken power-law density profile and different axial ratios R. The time t has been scaled by the diffusion time t_d as $\tau = t/t_d$ (Section 2.1), and the isotropic-equivalent luminosity $L(\tau; \mu, R)$ roughly takes a polar value in the direction $\mu = 0.95$ and an equatorial value in the direction $\mu = 0.05$. The thermalization time is $\tau_e = 10$. The dashed black vertical line shows the time to the peak of the light curve of the equivalent spherical ejecta ($R = 1$ with the same τ_e). The dashed colored curves show the fits using the functions in Equations (9) and (10). The bottom panel shows the error of the fits.

(a) Scaled by $L_n = Mq_0 t_{d,\text{day}}^{\sigma_1}$

(b) Scaled by $L_{\text{av}}(\tau; R)$

Figure 6. Isotropic-equivalent bolometric light curves $L(\tau, \mu; R)$ for an ellipsoid outflow with a constant density profile and axial ratio $R = 4$ at different viewing angles $\mu = \cos\theta$. The time t has been scaled by the diffusion time t_d as $\tau = t/t_d$, and the thermalization time is $\tau_e = 10$. (a) The isotropic-equivalent luminosity has been scaled by the factor $L_n = Mq_0 t_{d,\text{day}}^{\sigma_1}$ (Section 2.1). The solid black curve shows the angle-averaged luminosity, the dashed black curve shows the luminosity of the equivalent spherical ejecta ($R = 1$ with the same τ_e), and the dotted black curve shows the total heating rate. The dashed colored curves show the curve fits using the functions in Equations (9) and (10). The bottom panel shows the error of the fits. (b) The isotropic-equivalent luminosity has been scaled by the angle-averaged luminosity $L_{\text{av}}(\tau; R)$. The solid black horizontal line shows the angle-averaged luminosity. The bottom panel shows the error of $L(\tau, \mu_{\text{ref}}; R)$ from $L_{\text{av}}(\tau; R)$ for $\mu_{\text{ref}} = 0.55$.

The constant density case is similar to the broken power-law case, with some systematic differences. Figure 6 shows the isotropic-equivalent light curves for a constant density profile and an axial ratio $R = 4$ as an example. The light curves begin at a peak and decline monotonically, since the constant density ejecta has more mass at larger distances. The pole-to-equator projected area ratio again gives the rough scale of the luminosity variation at intermediate times. The relation $L(\tau, \mu_{\text{ref}}; R) \simeq L_{\text{av}}(\tau; R)$ has errors $\epsilon \lesssim 0.1$ for the reference value $\mu_{\text{ref}} = 0.55$. This suggests that μ_{ref} is a function primarily of the geometry. The relation $L_{\text{av}}(\tau; R) \simeq L_s(\tau)$ has an error $\epsilon < 0.1$ for $0.25 \leqslant R \leqslant 2$, rising to $\epsilon < 0.4$ for $R = 6$ (Figure B3). The fitting parameters $k(\tau; R)$ begin at lower values at early time but exhibit similar peak values and decline rates as the broken power-law case, and the analytic approximation for $k(\tau; R)$ has similar parameters (Figure B1). The projection factor then yields semianalytic light curves with errors of $\epsilon \lesssim 0.3$ for $0.25 \leqslant R \leqslant 2$, rising to $\epsilon \lesssim 0.8$ for $R = 6$.

The results here strictly apply only to an ellipsoidal geometry. However, since the light curves arise as an integration of the emission over the entire ejecta, they depend primarily on the global morphology and only weakly on small-scale distortions. The orientation effects of general, compact, contiguous geometries can thus be roughly estimated by considering a closely fitting ellipsoid with an effective axial ratio R_{eff}. In what follows, though, we analyze other geometries using the geometry-specific parallel projected area method, since this approach turns out to be fairly robust.

3.2. Torus

The light curves of a torus ejecta are analogous to those of an ellipsoid ejecta. In particular, we can explain the inclination

variation of the light curves using the same projected surface area method, with two main geometry-specific differences. The first is that the torus has a more complicated projected area (Appendix A.2). In particular, it has a characteristic break at $\pm\mu_{\text{break}} = \pm 1/K$, which corresponds to the viewing angle at which the torus begins to fully block the central hole. For $|\mu| \geqslant K^{-1/2}$, the torus does not block the hole; for $K^{-1} < |\mu| < K^{-1/2}$, it partially blocks the hole; and for $|\mu| \leqslant K^{-1}$, it fully blocks the hole. The projected area thus transitions from a shallower to a steeper dependence on viewing angle at $\mu = K^{-1}$ (Figure A1). The scale of the variation is again given by the pole-to-equator projected area ratio,

$$\frac{A_{\text{proj}}(\mu = 1; K)}{A_{\text{proj}}(\mu = 0; K)} = \frac{4\pi K}{4K + \pi}. \tag{11}$$

The second is that the torus has a different reference direction, $\mu_{\text{ref}} = 0.45$. The relation $L(\tau, \mu_{\text{ref}}; K) \simeq L_{\text{av}}(\tau; K)$ has errors $\epsilon \lesssim 0.1$ with this μ_{ref} for both the broken power-law and constant density profiles. As before, this suggests that μ_{ref} is a function primarily of the geometry.

To illustrate these differences, we present the signatures for a torus ejecta with a constant density profile and a radius ratio $K = 3$. Figure 7 shows the isotropic-equivalent light curves. Figure 8 shows the variation of the luminosity ratio $L(\tau, \mu; K)/L(\tau, \mu_{\text{ref}}; K)$ with viewing angle at different times.

The features shown in this specific case generalize to both density profiles (broken power-law and constant) and over our range of $K \in [1, 5]$ in a way analogous to the ellipsoid ejecta. The light curves in the broken power-law case have a rise-peak-fall time evolution. The relation $L_{\text{av}}(\tau; K) \simeq L_s(\tau)$ for the constant density case has errors $\epsilon \lesssim 0.2$ for $1 \leqslant K \leqslant 2$ rising to $\epsilon \lesssim 2.2$ for $K = 5$, and for the broken power-law case, it has

(a) **Scaled by** $L_n = M q_0 t_{d,\mathrm{day}}^{\sigma_1}$

(b) **Scaled by** $L_{\mathrm{av}}(\tau; K)$
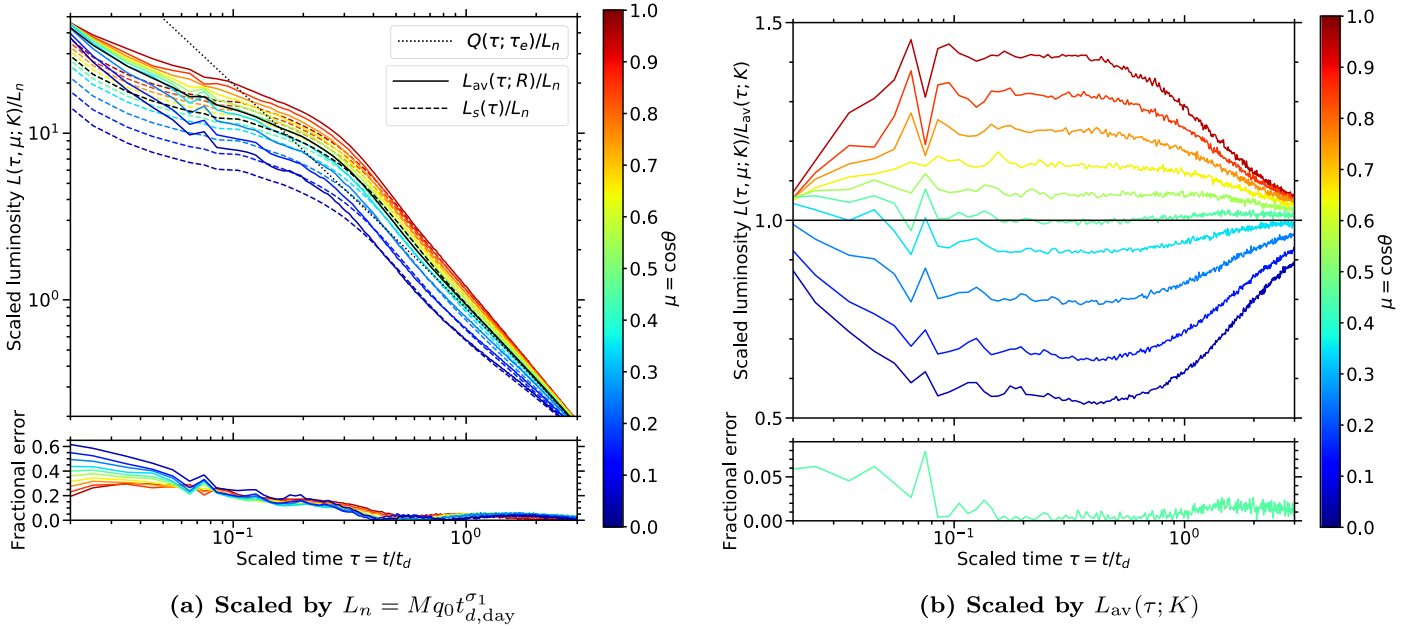
Figure 7. Isotropic-equivalent bolometric light curves $L(\tau, \mu; K)$ for a torus outflow with a constant density profile and radius ratio $K = 3$ at different viewing angles $\mu = \cos\theta$. The time t has been scaled by the diffusion time t_d as $\tau = t/t_d$, and the thermalization time is $\tau_e = 10$. (a) The isotropic-equivalent luminosity has been scaled by the factor $L_n = M q_0 t_{d,\mathrm{day}}^{\sigma_1}$ (Section 2.1). The solid black curve shows the angle-averaged luminosity, the dashed black curve shows the luminosity of the equivalent spherical ejecta (with the same M, E_k, and τ_e), and the dotted black curve shows the total heating rate. The dashed colored curves show the curve fits using the functions in Equations (9) and (10), with the replacement $R \rightarrow K$. The bottom panel shows the error of the fits. (b) The isotropic-equivalent luminosity has been scaled by the angle-averaged luminosity $L_{\mathrm{av}}(\tau; K)$. The solid black horizontal line shows the angle-averaged luminosity. The bottom panel shows the error of $L(\tau, \mu_{\mathrm{ref}}; K)$ from $L_{\mathrm{av}}(\tau; K)$ for $\mu_{\mathrm{ref}} = 0.45$.
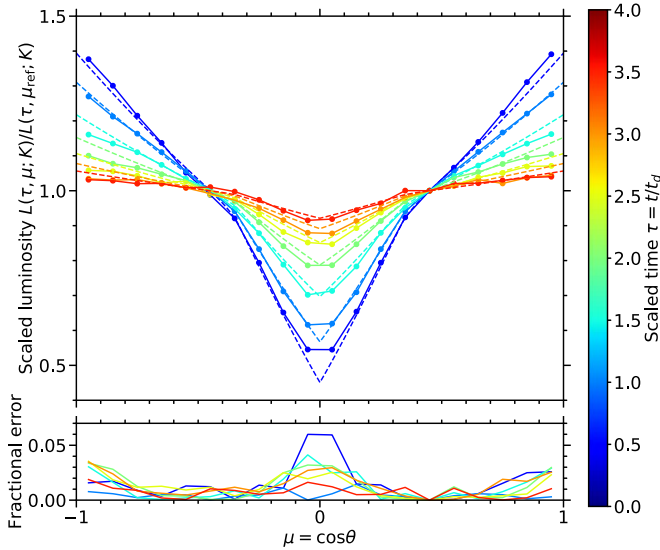
Figure 8. Isotropic-equivalent bolometric luminosities for a torus outflow with a constant density profile and radius ratio $K = 3$ as a function of viewing angle $\mu = \cos\theta$ at different times. The time t has been scaled by the diffusion time t_d as $\tau = t/t_d$ (Section 2.1), and the isotropic-equivalent luminosity $L(\tau, \mu; R)$ has been scaled by that in the reference direction $\mu_{\mathrm{ref}} = 0.45$, since in this direction, the luminosity roughly equals the angle-averaged luminosity. The torus has a constant density profile. The thermalization time is $\tau_e = 10$. The points and solid colored curves show the luminosities at different values of $\tau < 4$. The dashed colored curves show the fits to the function in Equation (9) with the replacement $R \rightarrow K$. The bottom panel shows the error of the fits.

errors $\epsilon \lesssim 0.3$ for $1 \leqslant K \leqslant 2$ rising to $\epsilon \lesssim 3.7$ for $K = 5$. The fitting parameters $k(\tau; K)$ have similar shapes but different values compared to the ellipsoidal case, and thus the analytic approximation for $k(\tau; K)$ has different values for $k_0(K)$ and $\tau_b(K)$ (Figure B2). It is interesting to compare the values for K

$\in [1, 5]$ to those for $R \in [2, 6]$, since they have similar degrees of asphericity; in general, the parameters k_0 and τ_b appear to depend on both the geometry and density profile. The semianalytic light curves for the broken power-law case have errors $\epsilon < 0.4$ for $1 \leqslant K \leqslant 2$ rising to $\epsilon < 0.8$ for $K = 5$, and those for the constant density case have errors $\epsilon < 0.55$ for $1 \leqslant K \leqslant 2$ rising to $\epsilon < 0.75$ for $K = 5$.

4. Discussion

The light curves presented here used ejecta models with idealized geometries and constant opacity to capture the effects of asymmetry. The idealized approach provides intuition for the fundamentally geometric effect that global asymmetry has on the light curves. Given that approximate models are frequently used to estimate kilonova light curves, the synthetic light curves presented here and the simple analytic prescriptions for them (Equations (9) and (10)) should be valuable for estimating the impact of asphericity and orientation.

We have focused here on the bolometric light curves of kilonovae and only marginally discussed their spectra and colors. However, the scale invariance of our models leads to dimensionless light curves, which we argued can serve as surrogates for the unobstructed emission produced by the different ejecta components, after reintroducing the appropriate scales of ejecta mass, opacity, and expansion velocity. Indeed, though the models used a uniform composition and a gray opacity, the resulting blackbody spectra provide a workable approximation of the colors. The colors are sensitive to the composition of the ejecta, tending to redder wavelengths when high-opacity lanthanide species are present (Kasen et al. 2013).

In general, though, kilonova ejecta have multiple interacting components, compositional inhomogeneities, and multiwavelength opacity. This structure implies that blocking,

reprocessing, and funneling effects, in addition to geometric effects, may also produce substantial color variation with viewing angle (Perego et al. 2014, 2017; Kasen et al. 2015, 2017; Kawaguchi et al. 2018, 2020; Wollaeger et al. 2018; Bulla 2019). The extent and efficacy of these depend on the spatial distribution and properties of the low-Y_e (lanthanide-rich, high opacity) material of dynamical origin and low- to high-Y_e (lanthanide-poor, low opacity) material of wind origin. For example, current dynamical simulations show that the lanthanide-rich material concentrates torus-like in the equatorial region and the lanthanide-poor material concentrates cone-like in the polar regions (e.g., Radice et al. 2018b). If the lanthanide-rich material has a larger radius and expansion velocity than the lanthanide-poor material, then the former can modify the blue emission from the latter: blocking inhibits the emission from penetrating along the equator (Kasen et al. 2015, 2017; Kawaguchi et al. 2018, 2020; Wollaeger et al. 2018; Bulla 2019); reprocessing shifts the observed photosphere to larger radii and velocities, reduces the effective temperatures and frequencies, and isotropizes the direction (Perego et al. 2017; Kawaguchi et al. 2018, 2020; Bulla 2019); and funneling redirects the diffusing photons in the polar direction (Kawaguchi et al. 2020). The aggregate result is that the blue emission is obscured in the equatorial direction, and thus bluer spectra are observed at near-polar angles and redder spectra at near-equatorial angles. In contrast, if the lanthanide-rich material is enshrouded in lanthanide-poor material, then analogously, the red emission from the former is reprocessed into blue emission and isotropized (Kawaguchi et al. 2020).

More simply, we can use the projected surface area approach to make a rough estimate of the impact of geometry and blocking from this ejecta. We model the outflow as a cone of low-opacity ejecta with a half-opening angle $\theta_c \in [0, \pi/2]$ embedded inside a high-opacity sphere of radius a (Figure 1). In this model, only the polar "caps" of the low-opacity cone will be visible, as the interior is obscured by the high-opacity lanthanide-rich envelope. The projected surface area $A_{\mathrm{proj}}^{\mathrm{caps}}(\mu; \mu_c)$ of the caps then provides a rough estimate of the viewing angle dependence of the blue light curve, while that for the red light curve can be described by the complementary geometry $A_{\mathrm{proj}}^{\mathrm{comp}}(\mu; \mu_c) = \pi a^2 - A_{\mathrm{proj}}^{\mathrm{caps}}(\mu; \mu_c)$.

Appendix A.3 gives analytic formulae for the projected surface area of the conical caps, and Figure A1 shows the variation of the area with viewing angle. The results indicate that the blue light curve will be brighter for polar viewing angles where the cap is fully visible and dimmer for equatorial ones where only a small region of the cap is visible. The pole-to-equator projected area ratio has the simple analytic expression

$$\frac{A_{\mathrm{proj}}(\mu = 1; \mu_c)}{A_{\mathrm{proj}}(\mu = 0; \mu_c)} = \frac{\pi \sin^2 \theta_c}{2(\theta_c - \sin \theta_c \cos \theta_c)}. \quad (12)$$

For a typical conical opening angle $\theta_c \approx 45°$ ($\mu_c \approx 0.71$) (Radice et al. 2018b), the projected area ratio is ≈ 2.8. We thus expect the blue luminosity to vary by a factor of ~ 3–5 with viewing angle at peak, consistent with prior detailed transport models (Kasen et al. 2015; Kawaguchi et al. 2018, 2020; Wollaeger et al. 2018; Bulla 2019). For smaller opening angles $\theta_c \approx 20°$ ($\mu_c \approx 0.94$), the variation can be a factor of ~ 5–10 at peak, i.e., up to an order of magnitude. While detailed calculations are needed for quantitative modeling, this

semianalytic approach using the projected surface area roughly gauges the size of the geometric effects. A similar approach could presumably be used for modified geometries as well. For instance, this conical cap model assumes the lanthanide-poor and lanthanide-rich materials have a comparable radial extent, whereas a modified setup could potentially accommodate two different component velocities.

The results in this paper suggest potential diagnostics for inferring the orientation angle from kilonova observations. As the orientation of a merging binary system is only partially constrained by its GW signal, a complementary constraint from kilonova observations would be of considerable interest. Since the inclination dependence of the light curves diminishes with time, the ratio of the luminosity on the light-curve tail to that at peak is highly correlated with orientation, as shown in Figure 9. The tail-to-peak ratio declines more rapidly for viewing angles with larger projected areas, since these have higher peaks and must converge to the total heating rate $Q(\tau; \tau_e)$ at late times. The ratio of curves of different μ at late times equals the ratio of their peak luminosities $L_p(\mu; R)$. Ejecta with higher R have a larger spread in decline rates, since the projected area changes more from pole to equator.

The tail-to-peak luminosity ratio thus provides a potential way to constrain the outflow geometry and inclination. However, the luminosity ratio is partly degenerate with other inputs, such as the heating rate (Figure 9), which complicates efforts to use the light curve alone to infer the ejecta geometry or the underlying radioactivity and thermalization. It remains to be seen the extent to which multiparameter fitting of the light curves can individually constrain the parameters.

The parameters (mass, velocity, etc.) of the blue and red components of GW170817/AT 2017gfo were inferred by fitting the observed light curves with synthetic ones from spherically symmetric models (Chornock et al. 2017; Cowperthwaite et al. 2017; Nicholl et al. 2017; Kasen et al. 2017; Tanaka et al. 2017). Aspherical models would generally lead to different inferred parameters. To quantify the size of the difference, we compare a spherical model (with parameters labeled with the subscript s) to ellipsoidal models with axial ratios $R = 1/2$ and 2, which encapsulate the two directions the asphericity might tend. Indeed, the red component likely comes from the postmerger disk wind, which is mildly prolate, but the source of the blue component is more uncertain and could arise from the dynamical ejecta or more hypothetical outflows (Metzger 2017). We use the current estimates for the viewing angle, $\theta \approx 30°$ ($\mu \approx 0.87$; Finstad et al. 2018; Abbott et al. 2019; Wu & MacFadyen 2019). We then infer the mass, opacity, velocity, and thermalization time that yield the same peak and late-time behavior in the physical light curve as in the spherical case. For $R = 1/2$, we find $M \sim 1.4 M_s$ (i.e., $\sim 40\%$ larger than the spherical case), $\kappa/\beta_{\mathrm{ch}} \sim 0.7(\kappa/\beta_{\mathrm{ch}})_s$, and $\tau_e \sim 0.8 (\tau_e)_s$. For $R = 2$, we find $M \sim 0.6 M_s$ (i.e., $\sim 40\%$ smaller than the spherical case), $\kappa/\beta_{\mathrm{ch}} \sim 1.7(\kappa/\beta_{\mathrm{ch}})_s$, and $\tau_e \sim 1.5 (\tau_e)_s$. The mass uncertainties from geometric effects of this magnitude are a factor of $\lesssim 2$ and comparable to those from uncertainties in the ejecta opacities (Barnes & Kasen 2013) and the heating rate (Metzger et al. 2010; Korobkin et al. 2012; Lippuner & Roberts 2015).

In BH–NS mergers, the tidal component of the dynamical ejecta can be highly asymmetric. In general terms, if the binary has a low mass ratio, the BH has high aligned spin, and the NS has low compactness, then tidal disruption can occur far
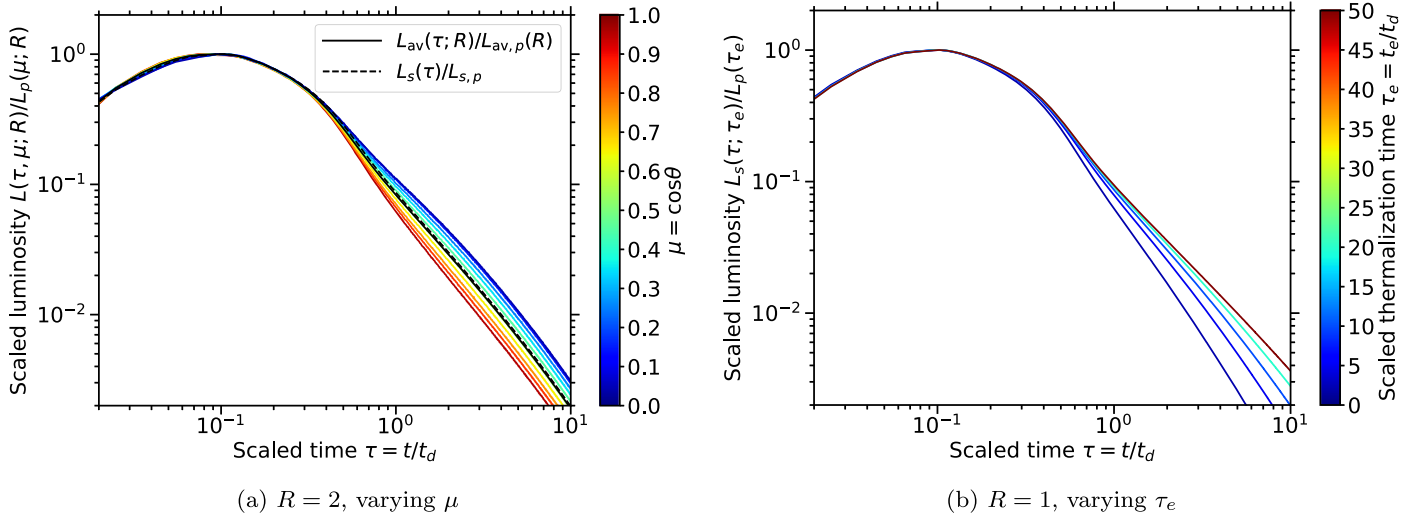
Figure 9. (a) Isotropic-equivalent bolometric light curves for an ellipsoid outflow with axial ratio $R = 2$ at different viewing angles $\mu = \cos\theta$. The time t has been scaled by the diffusion time t_d as $\tau = t/t_d$ (Section 2.1), and the isotropic-equivalent luminosity $L(\tau, \mu; R)$ has been scaled by its peak value $L_p(\mu; R)$. The solid black curve shows the angle-averaged luminosity, and the dashed black curve shows the luminosity of the equivalent spherical ejecta ($R = 1$ with the same τ_e). (b) Bolometric light curve of a spherical outflow with different thermalization times $\tau_e = t_e/t_d$. The luminosity has been scaled by its peak value $L_p(\tau_e)$. We note that $L_p(\tau_e)$ varies little for the values of τ_e shown, since they satisfy $\tau_e \gg \tau_p(\mu; R) \sim 0.1$. A comparison of the two panels shows that there is some degeneracy between observing (1) an ellipsoidal outflow at different viewing angles and (2) a spherical outflow with different heating rates, though the two may be distinguishable by careful measurement of the power-law decline at late times.

outside the BH horizon, leading to a single tidal tail concentrated in the equatorial plane ($v_x/v_z \sim 5$) with a limited azimuthal range ($\Delta\phi \lesssim \pi$; Foucart et al. 2013, 2019; Kyutoku et al. 2015). Though this is a typical case, the detailed properties of the tidal tail and the fraction of unbound mass depend sensitively on the particulars of the merger, such as the BH spin alignment and the NS equation of state (Kawaguchi et al. 2015; Kyutoku et al. 2015; Foucart et al. 2017). We can roughly model the tidal tail as an ellipsoid with axial ratio $R = 5$ or a torus with radius ratio $K = 5$. The luminosity variation with polar viewing angle is then roughly a factor of $\sim$5–10 near peak before reducing to $\sim$1 at late times. Global geometric effects are thus important inputs to accurately constrain the mass ejected from these systems.

Appendix A
Projected Area

In this appendix, we present equations for the parallel projected areas of the ejecta geometries studied in the paper (Figure 1): an ellipsoid, a ring torus, and a conical cap. The geometries are axisymmetric, so we parameterize the viewing angle with $\mu = \cos\theta$, where θ is the polar angle. Figure A1

shows the projected areas as a function of μ, normalized to their values at $\mu = \pm 1$.

A.1. Ellipsoid

We study an ellipsoid with semimajor axes (a_x, a_y, a_z), where $a_x = a_y$ (axisymmetric, spheroid), and we define the axial ratio $R = a_x/a_z$ (Figure 1). A straightforward analysis of the geometry shows that the parallel projected area of the ellipsoid in the direction μ is an ellipse with semimajor axes $(a_x, a_z[(R^2 - 1)\mu^2 + 1]^{1/2})$. The parallel projected area in the direction μ is thus

$$A_{\text{proj}}(\mu; R) = \pi R a_z^2 [(R^2 - 1)\mu^2 + 1]^{1/2}. \quad (A1)$$

Figure A1 shows a plot of $A_{\text{proj}}(\mu; R)$. The pole-to-equator ratio is

$$\frac{A_{\text{proj}}(\mu = 1; R)}{A_{\text{proj}}(\mu = 0; R)} = R. \quad (A2)$$

A.2. Torus

We study a torus with spine radius a_c and tube radius a_t, where $a_c > a_t$ (ring torus), and we define the radius ratio $K = a_c/a_t \geq 1$ (Figure 1). A straightforward analysis of the geometry shows that the parallel projected area of the torus in the direction μ is the area bounded by the parallel curves of an ellipse with semimajor axes $(a_c, a_c \mu)$. The outer ($+$) and inner ($-$) parallel curves can be expressed with the parametric equations

$$\tilde{x}(t) = a_t\left(K \pm \frac{\mu}{(1 - (1 - \mu^2)\cos^2 t)^{1/2}}\right)\cos t, \quad (A3)$$

$$\tilde{y}(t) = a_t\left(K\cos\theta \pm \frac{1}{(1 - (1 - \mu^2)\cos^2 t)^{1/2}}\right)\sin t. \quad (A4)$$
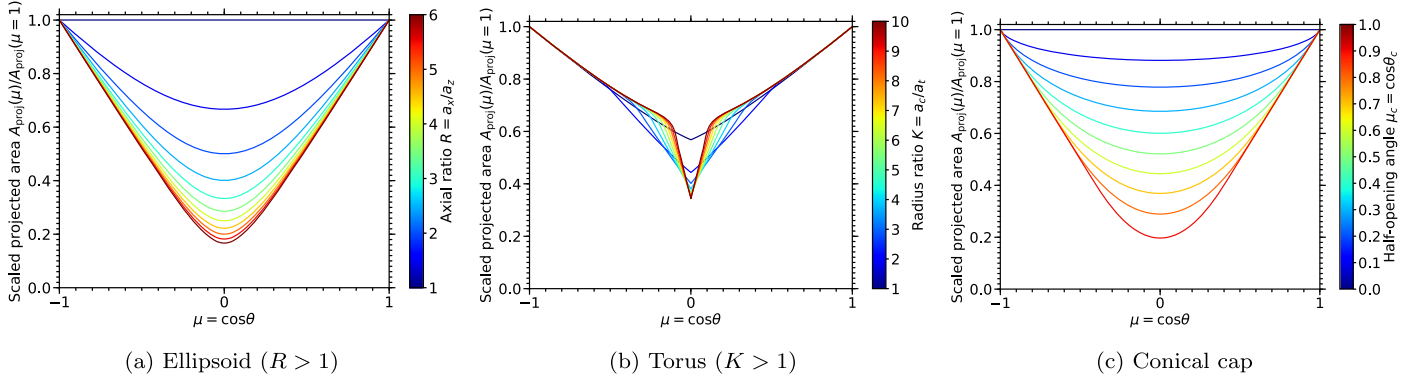
Figure A1. Analytic projected area $A_{\text{proj}}(\mu; R)$ for several axisymmetric geometries. The panels show the projected area for (a) an ellipsoid with axial ratio $R = a_x/a_z > 1$, (b) a ring torus with radius ratio $K = a_c/a_t > 1$, and (c) two conical caps with half-opening angle $\mu_c \in [0,1]$. Equations for the analytic functions $A_{\text{proj}}(\mu)$ are given in the text (Appendix A).

The parallel projected area in the direction μ can be written as

$$A_{\text{proj}}(\mu; K) = A_{\text{outer}}(\mu; K) - A_{\text{inner}}(\mu; K), \qquad (A5)$$

where $A_{\text{outer}}(\mu; K)$ and $A_{\text{inner}}(\mu; K)$ are the areas contained inside the outer and inner parallel curves, respectively. The following integrals will be useful for evaluating these areas:

$$I_1(t_1, t_2) = \int_{t_1}^{t_2} \sin^2 t\, dt, \qquad (A6)$$

$$I_2(\mu; t_1, t_2) = \int_{t_1}^{t_2} \frac{\sin^2 t}{(1 - (1 - \mu^2)\cos^2 t)^{3/2}} dt, \qquad (A7)$$

$$I_3(\mu; t_1, t_2) = \int_{t_1}^{t_2} \frac{\sin^2 t}{(1 - (1 - \mu^2)\cos^2 t)^{1/2}} dt, \qquad (A8)$$

$$I_4(\mu; t_1, t_2) = \int_{t_1}^{t_2} \frac{\sin^2 t}{(1 - (1 - \mu^2)\cos^2 t)^2} dt. \qquad (A9)$$

We note that $I_1(0, \pi) = \pi/2$ and $I_4(\mu; 0, \pi) = \pi/2|\mu|$. The outer projected area can be written as

$$A_{\text{outer}}(\mu; K) = 2a_t^2 [K^2|\mu|I_1(0, \pi) + K\mu^2 I_2(\mu; 0, \pi) \\ + KI_3(\mu; 0, \pi) + |\mu|I_4(\mu; 0, \pi)]. \qquad (A10)$$

The form of the inner projected area depends on the range of μ: for different μ, the torus blocks the central hole to a different degree, which leads to a different degree of overlap of the inner parallel curve with itself. The inner projected area can be divided into three domains as follows.

1. $|\mu| \geqslant K^{-1/2}$: no blocking/overlap,

$$A_{\text{inner}}(\mu; K) = 2a_t^2 [K^2|\mu|I_1(0, \pi) - K\mu^2 I_2(\mu; 0, \pi) \\ - KI_3(\mu; 0, \pi) + |\mu|I_4(\mu; 0, \pi)]. \qquad (A11)$$

2. $K^{-1/2} > |\mu| > K^{-1}$: partial blocking/overlap,

$$A_{\text{inner}}(\mu; K) = 2a_t^2 [K^2|\mu|I_1(t_r, \pi - t_r) \\ - K\mu^2 I_2(\mu; t_r, \pi - t_r) - KI_3(\mu; t_r, \pi - t_r) \\ + |\mu|I_4(\mu; t_r, \pi - t_r)], \qquad (A12)$$

where $t_r(\mu; K) = \cos^{-1}((1 - \mu^2)^{-1/2}[1 - K^{-2}\mu^{-2}]^{1/2})$.
3. $K^{-1} \geqslant |\mu|$: full blocking/overlap,

$$A_{\text{inner}}(\mu; K) = 0. \qquad (A13)$$

All of the integrals above can be evaluated either explicitly or in terms of elliptic integrals. Figure A1 shows a plot of $A_{\text{proj}}(\mu; K)$. The curves show a characteristic break at $\pm\mu_{\text{break}} = \pm 1/K$, which corresponds to the viewing angle at which the torus begins to fully block the central hole. The pole-to-equator ratio is

$$\frac{A_{\text{proj}}(\mu = 1; K)}{A_{\text{proj}}(\mu = 0; K)} = \frac{4\pi K}{4K + \pi}. \qquad (A14)$$

A.3. Conical Cap

We study a cone with a half-opening angle $\theta_c \in [0, \pi/2]$ ($\mu_c = \cos\theta_c \in [0, 1]$) embedded inside a sphere of radius a (Figure 1). The parallel projected area has a different form depending on the viewing angle and can be divided into four domains. In the interval $-(1 - \mu_c^2)^{1/2} < \mu < (1 - \mu_c^2)^{1/2}$, the following variables will be useful:

$$\theta_p(\mu; \mu_c) = \cos^{-1}\left(\frac{\mu_c}{(1 - \mu^2)^{1/2}}\right) \in [0, \theta_c], \qquad (A15)$$

$$\theta_d(\mu; \mu_c) = \tan^{-1}\left(\frac{\sin\theta_p}{\mu_c}\frac{(1 - \mu^2)^{1/2}}{|\mu|}\right) \in \left[0, \frac{\pi}{2}\right]. \qquad (A16)$$

The parallel projected area of the top and bottom caps together, when the rest of the cone is blocked by the sphere, can be written as

$$A_{\text{proj}}(\mu; \mu_c) = A_{\text{proj}}^{\text{top}}(\mu; \mu_c) + A_{\text{proj}}^{\text{top}}(-\mu; \mu_c), \qquad (A17)$$

where $A_{\text{proj}}^{\text{top}}(\mu; \mu_c)$ is the parallel projected area of the top cap alone, when the rest of the cone is blocked by the sphere, which takes the following form in the four domains.

1. $1 \geqslant \mu \geqslant (1 - \mu_c^2)^{1/2}$:

$$A_{\text{proj}}^{\text{top}}(\mu; \mu_c) = \pi a^2 (1 - \mu_c^2)\mu. \qquad (A18)$$

2. $(1 - \mu_c^2)^{1/2} > \mu \geqslant 0$:

$$A_{\text{proj}}^{\text{top}}(\mu; \mu_c) = a^2(\theta_p - \sin\theta_p \cos\theta_p) \\ - a^2(1 - \mu_c^2)^{1/2}\mu(\theta_d - \sin\theta_d \cos\theta_d - \pi). \qquad (A19)$$

3. $0 > \mu > -(1 - \mu_c^2)^{1/2}$:

$$A_{\text{proj}}^{\text{top}}(\mu; \mu_c) = a^2(\theta_{\text{p}} - \sin\theta_{\text{p}}\cos\theta_{\text{p}})$$
$$+ a^2(1 - \mu_c^2)^{1/2}\mu(\theta_{\text{d}} - \sin\theta_{\text{d}}\cos\theta_{\text{d}}). \quad (A20)$$

4. $-(1 - \mu_c^2)^{1/2} \geqslant \mu \geqslant -1$:

$$A_{\text{proj}}^{\text{top}}(\mu; \mu_c) = 0. \quad (A21)$$

Figure A1 shows a plot of $A_{\text{proj}}(\mu; \mu_c)$. The pole-to-equator ratio is

$$\frac{A_{\text{proj}}(\mu = 1; \mu_c)}{A_{\text{proj}}(\mu = 0; \mu_c)} = \frac{\pi\sin^2\theta_c}{2(\theta_c - \sin\theta_c\cos\theta_c)}. \quad (A22)$$

Appendix B
Additional Features of the Light Curves

The projection factor presented in Section 3 involves several approximations and parameters. Here we present data on the size of the approximations and the values of the parameters and quantify their limitations and domains of applicability. We present the data for both geometries (ellipsoid and torus) and density profiles (broken power-law and constant) but focus in the text on an ellipsoid kilonova.

B.1. Analytic Approximation for k

Figure B1 shows the fitting parameter $k(\tau; R)$ from Equation (9) for an ellipsoid outflow over our range $R \in [0.25, 6]$. The curves have a similar behavior for different R. They rise to peak values >1 at times $\tau \lesssim 1$ and then decay to zero roughly exponentially. The ejecta with higher R take longer to converge. Figure B1 also shows the fitting parameters $k_0(R)$ and $\tau_b(R)$ from the analytic approximation to $k(\tau; R)$ given in Equation (10). We find that the constant values $k_0(R) \simeq 1.2$ and $\tau_b(R) \simeq 0.7$ yield semianalytic light curves with errors $\epsilon < 0.2$ for $0.25 \leqslant R \leqslant 2$ rising to $\epsilon < 0.6$ for $R = 6$.

The light curves $L(\tau, \mu; R) > 0$, and thus $k(\tau; R)$, must lie in the range $0 \leqslant k(\tau; R) < k_{\text{upper}}(\tau; R)$, where $k_{\text{upper}}(\tau; R) = (1 - \min_\mu A_{\text{proj}}(\mu; R)/A_{\text{proj}}(\mu_{\text{ref}}; R))^{-1}$. The lower bound

ensures that the semianalytic approximation for $L(\tau, \mu; R)$ in Equation (9) satisfies $L(\tau, \mu_1; R) > L(\tau, \mu_2; R)$ when $A_{\text{proj}}(\mu_1; R) > A_{\text{proj}}(\mu_2; R)$, and the upper bound ensures that it satisfies $L(\tau, \mu; R) > 0$ when $A_{\text{proj}}(\mu; R)/A_{\text{proj}}(\mu_{\text{ref}}; R) < 1$.

An analytic approximation for $k(\tau; R)$ should remain within the above bounds as well. However, the expression given in Equation (10) increases monotonically with decreasing τ and can potentially surpass $k_{\text{upper}}(\tau; R)$ at early times if the fitting parameters $k_0(R)$ and $\tau_b(R)$ are chosen carelessly and thereby produce negative values for $L(\tau, \mu; R)$. This additional constraint can potentially restrict the range of R over which the analytic approximation is accurate. The values for $k_0(R)$ and $\tau_b(R)$ given above preserve a positive value for $L(\tau, \mu; R)$.

The torus outflow has analogous results, shown in Figure B2.

B.2. Comparison of L_{av} and L_s

Figure B3 shows the curves $L_{av}(\tau; R)/L_s(\tau)$ for an ellipsoid outflow over our range $R \in [0.25, 6]$, which we can examine to quantify the deviation of $L_{av}(\tau; R)$ from $L_s(\tau)$. There is a time $\tau_{\text{cr}}(R)$ at which $L_{av}(\tau; R)/L_s(\tau) = 1$, i.e., where $L_{av}(\tau; R)$ and $L_s(\tau)$ cross, and it falls in the range $0.3 \leqslant \tau_{\text{cr}}(R) \leqslant 0.37$. For $\tau > \tau_{\text{cr}}(R)$, $L_{av}(\tau; R)$ and $L_s(\tau)$ differ by an error $\epsilon < 0.2$, and we can roughly take $L(\tau; R)/L_s(\tau) \simeq 1$. For $\tau < \tau_{\text{cr}}(R)$, $L_{av}(\tau; R)$ is larger than $L_s(\tau)$, and the deviation is greater for ejecta with higher R. This is because photons can escape more easily in the z-direction for the ellipsoidal ejecta, leading to a lower effective diffusion time. In this region, we can roughly take $L_{av}(\tau; R)/L_s(\tau) \simeq 1$ for $R \lesssim 3$, since we only incur an error $\epsilon < 0.2$, but we should use a more accurate expression for $R \gtrsim 3$. It is important to be accurate in this region, since the light curves experience their peak here.

Motivated by this behavior, we adopt the following analytic approximation:

$$\frac{L_{av}(\tau; R)}{L_s(\tau)} \simeq 1 + \alpha(R)e^{-\tau^2/\tau_g^2(R)}. \quad (B1)$$

Here $\alpha(R)$ is the amplitude and $\tau_g(R)$ is the decay time, which falls in the range $\tau_g(R) \lesssim \tau_{\text{cr}}(R)$. The function thus provides a fit in the region $\tau \lesssim \tau_{\text{cr}}(R)$ and is $L_{av}(\tau; R)/L_s(\tau) \simeq 1$ in the region $\tau \gtrsim \tau_{\text{cr}}(R)$. Figure B3 shows the fitting parameters $\alpha(R)$ and $\tau_g(R)$ obtained from fitting the curves $L_{av}(\tau; R)/L_s(\tau)$

(a) Broken power law   (b) Constant   (c) Parameters
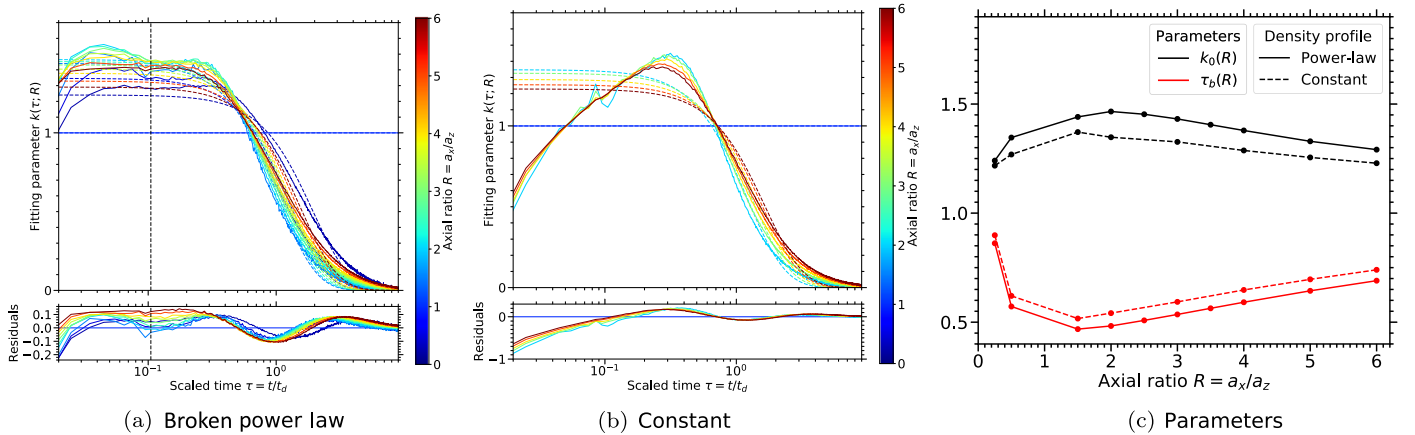
Figure B1. (a) and (b) Fitting parameter $k(\tau; R)$ in Equation (9) for an ellipsoid outflow with the two density profiles studied in the paper (Section 2.2): (a) a broken power law and (b) a constant. The colors show different axial ratios $R = a_x/a_z$. The time t has been scaled by the diffusion time t_d as $\tau = t/t_d$ (Section 2.1). The dashed black vertical line shows the time to peak of the light curve of the equivalent spherical ejecta ($R = 1$ with the same τ_e). The dashed colored curves show the fits to the analytic approximation given in Equation (10), and the bottom panels show the residuals of the fits. (c) Parameters $k_0(R)$ (black) and $\tau_b(R)$ (red) for the broken power-law (solid) and constant (dashed) density profiles.

(a) Broken power law   (b) Constant   (c) Parameters
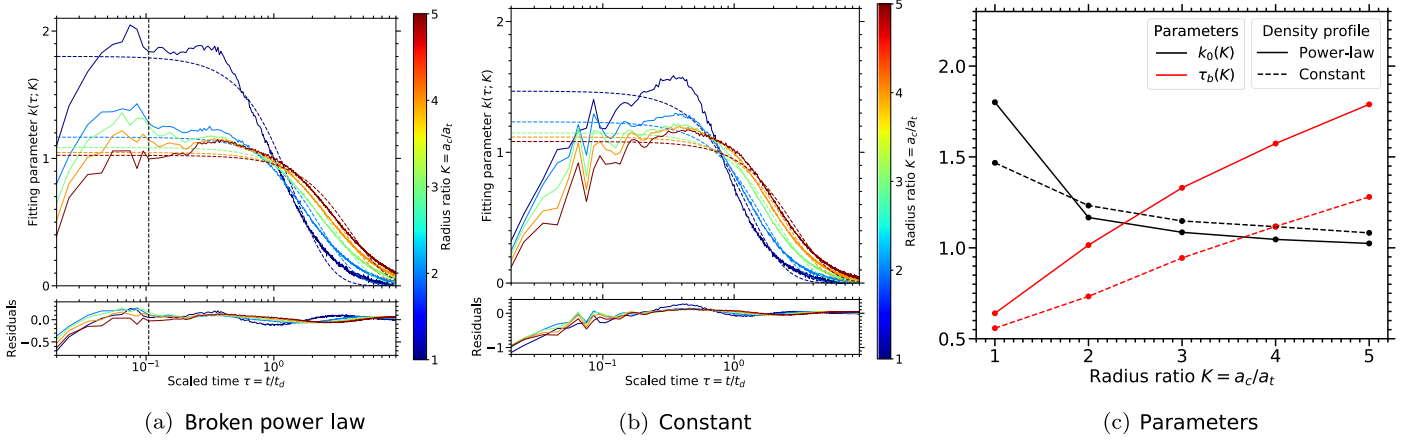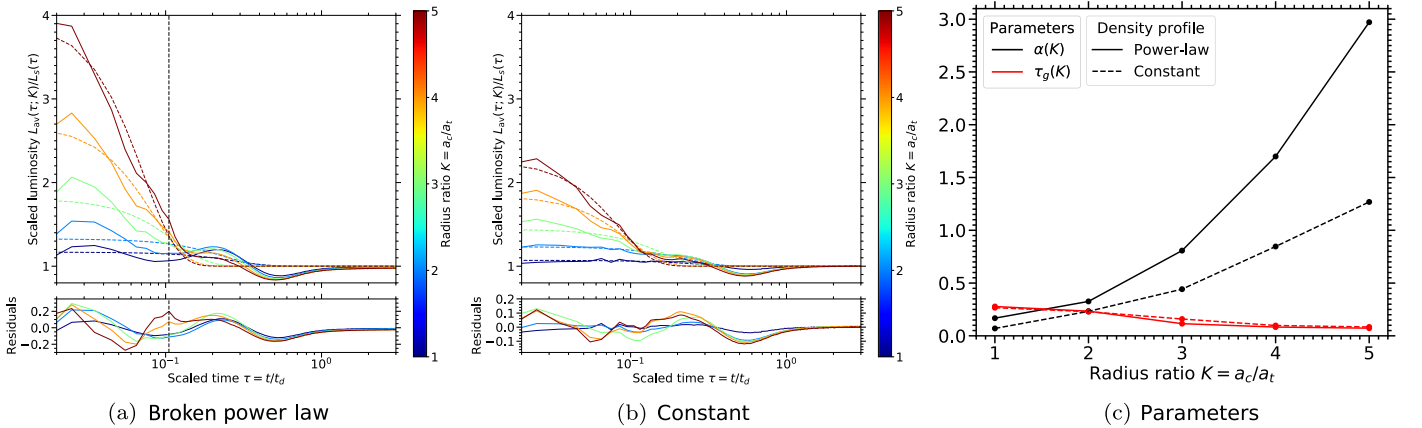
Figure B2. (a) and (b) Fitting parameter $k(\tau; K)$ in Equation (9) for a torus outflow with the two density profiles studied in the paper (Section 2.2): (a) a broken power law and (b) a constant. The colors show different radius ratios $K = a_c/a_t$. The time t has been scaled by the diffusion time t_d as $\tau = t/t_d$ (Section 2.1). The dashed black vertical line shows the time to the peak of the light curve of the equivalent spherical ejecta (with the same M, E_k, and τ_e). The dashed colored curves show the fits to the analytic approximation given in Equation (10), and the bottom panels show the residuals of the fits. (c) Parameters $k_0(K)$ (black) and $\tau_b(K)$ (red) for the broken power-law (solid) and constant (dashed) density profiles.

(a) Broken power law   (b) Constant   (c) Parameters
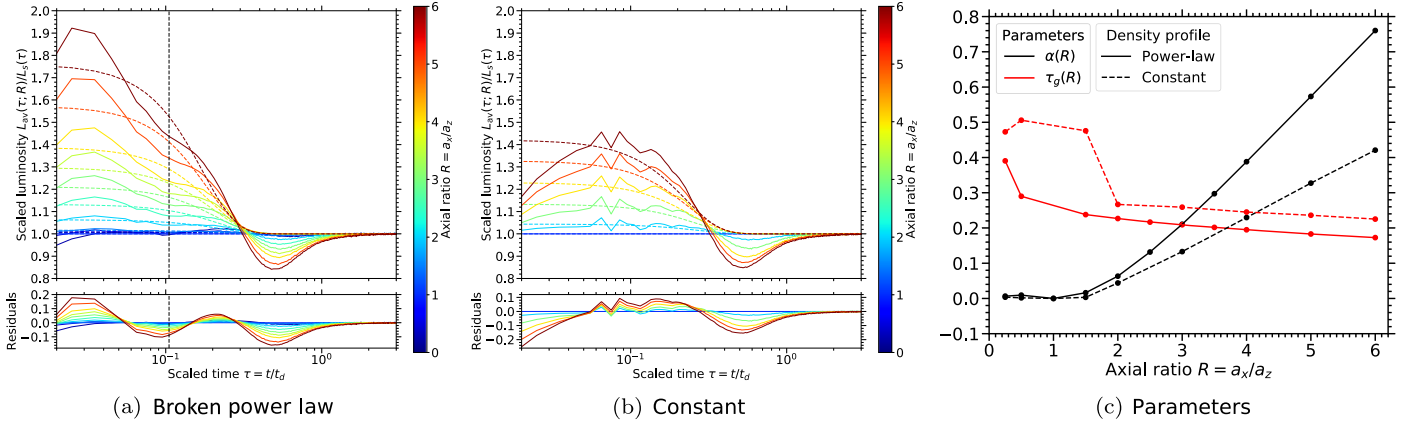
Figure B3. (a) and (b) Angle-averaged bolometric light curves for an ellipsoid outflow with the two density profiles studied in the paper (Section 2.2): (a) a broken power law and (b) a constant. The colors show different axial ratios $R = a_{ax}/a_z$. The time t has been scaled by the diffusion time t_d as $\tau = t/t_d$ (Section 2.1), and the angle-averaged luminosity $L_{av}(\tau; R)$ has been scaled by the luminosity $L_s(\tau)$ of the equivalent spherical ejecta ($R = 1$ with the same τ_e). The dashed black vertical line shows the time to the peak of the light curve of the equivalent spherical ejecta. The dashed colored curves show the fits to the function in Equation (B1), and the bottom panel shows the residuals of the fits. (c) Parameters $\alpha(R)$ (black) and $\tau_g(R)$ (red) for the broken power-law (solid) and constant (dashed) density profiles.

(a) Broken power law   (b) Constant   (c) Parameters

Figure B4. (a) and (b) Angle-averaged bolometric light curves for a torus outflow with the two density profiles studied in the paper (Section 2.2): (a) a broken power law and (b) a constant. The colors show different radius ratios $K = a_c/a_t$. The time t has been scaled by the diffusion time t_d as $\tau = t/t_d$ (Section 2.1), and the angle-averaged luminosity $L_{av}(\tau; K)$ has been scaled by the luminosity $L_s(\tau)$ of the equivalent spherical ejecta (with the same M, E_k, and τ_e). The dashed black vertical line shows the time to the peak of the light curve of the equivalent spherical ejecta. The dashed colored curves show the fits to the function in Equation (B1), and the bottom panel shows the residuals of the fits. (c) Parameters $\alpha(K)$ (black) and $\tau_g(K)$ (red) for the broken power-law (solid) and constant (dashed) density profiles.

with $g(\tau; R)$. For $R \lesssim 3$, we can approximate $L_{\mathrm{av}}(\tau;R)/L_s(\tau) \simeq 1$, incurring an error of $\epsilon \lesssim 0.2$ for all τ. For $R \gtrsim 3$, one should use the full expression for $L_{\mathrm{av}}(\tau; R)/L_s(\tau)$ if an error $\lesssim 0.2$ is needed.

We can thus obtain a more accurate projection factor from $L_s(\tau)$ to $L(\tau, \mu; R)$ by combining Equations (9) (with the replacement $L(\tau, \mu_{\mathrm{ref}}; R) \to L_{\mathrm{av}}(\tau; R)$), (B1), and (10). This parameterization is more involved. The numerical models are also available if accurate light curves are needed.

The torus outflow has analogous results, shown in Figure B4.

References

Abbott, B. P., Abbott, R., Abbott, T. D., et al. 2017a, PhRvL, 119, 161101
Abbott, B. P., Abbott, R., Abbott, T. D., et al. 2017b, ApJL, 848, L12
Abbott, B. P., Abbott, R., Abbott, T. D., et al. 2017c, Natur, 551, 85
Abbott, B. P., Abbott, R., Abbott, T. D., et al. 2019, PhRvX, 9, 011001
Arcavi, I., Hosseinzadeh, G., Howell, D. A., et al. 2017, Natur, 551, 64
Arnett, W. D. 1982, ApJ, 253, 785
Barbieri, C., Salafia, O. S., Perego, A., Colpi, M., & Ghirlanda, G. 2019, A&A, 625, A152
Barnes, J., & Kasen, D. 2013, ApJ, 775, 18
Barnes, J., Kasen, D., Wu, M.-R., & Martínez-Pinedo, G. 2016, ApJ, 829, 110
Bauswein, A., Goriely, S., & Janka, H. T. 2013, ApJ, 773, 78
Bulla, M. 2019, MNRAS, 489, 5037
Chevalier, R. A., & Soker, N. 1989, ApJ, 341, 867
Chornock, R., Berger, E., Kasen, D., et al. 2017, ApJL, 848, L19
Coughlin, M. W., Dietrich, T., Heinzel, J., et al. 2020, PhRvR, 2, 022006
Coulter, D. A., Foley, R. J., Kilpatrick, C. D., et al. 2017, Sci, 358, 1556
Cowperthwaite, P. S., Berger, E., Villar, V. A., et al. 2017, ApJL, 848, L17
Dietrich, T., Ujevic, M., Tichy, W., Bernuzzi, S., & Brügmann, B. 2017, PhRvD, 95, 024029
Drout, M. R., Piro, A. L., Shappee, B. J., et al. 2017, Sci, 358, 1570
Eichler, D., Livio, M., Piran, T., & Schramm, D. N. 1989, Natur, 340, 126
Evans, P. A., Cenko, S. B., Kennea, J. A., et al. 2017, Sci, 358, 1565
Feeney, S. M., Peiris, H. V., Williamson, A. R., et al. 2019, PhRvL, 122, 061105
Fernández, R., Tchekhovskoy, A., Quataert, E., Foucart, F., & Kasen, D. 2019, MNRAS, 482, 3373
Finstad, D., De, S., Brown, D. A., Berger, E., & Biwer, C. M. 2018, ApJL, 860, L2
Fishbach, M., Gray, R., Magaña Hernandez, I., et al. 2019, ApJ, 871, L13
Foucart, F., Deaton, M. B., Duez, M. D., et al. 2013, PhRvD, 87, 084006
Foucart, F., Desai, D., Brege, W., et al. 2017, CQGra, 34, 044002
Foucart, F., Duez, M. D., Kidder, L. E., et al. 2019, PhRvD, 99, 103025
Freiburghaus, C., Rosswog, S., & Thielemann, F.-K. 1999, ApJL, 525, L121
Fujibayashi, S., Kiuchi, K., Nishimura, N., Sekiguchi, Y., & Shibata, M. 2018, ApJ, 860, 64
Grossman, D., Korobkin, O., Rosswog, S., & Piran, T. 2014, MNRAS, 439, 757
Hotokezaka, K., Kiuchi, K., Kyutoku, K., et al. 2013, PhRvD, 87, 024001
Hotokezaka, K., Nakar, E., Gottlieb, O., et al. 2019, NatAs, 3, 940
Hotokezaka, K., Sari, R., & Piran, T. 2017, MNRAS, 468, 91
Kasen, D., Badnell, N. R., & Barnes, J. 2013, ApJ, 774, 25
Kasen, D., & Barnes, J. 2019, ApJ, 876, 128
Kasen, D., Fernández, R., & Metzger, B. D. 2015, MNRAS, 450, 1777
Kasen, D., Metzger, B., Barnes, J., Quataert, E., & Ramirez-Ruiz, E. 2017, Natur, 551, 80
Kasen, D., Thomas, R. C., & Nugent, P. 2006, ApJ, 651, 366
Kasliwal, M. M., Nakar, E., Singer, L. P., et al. 2017, Sci, 358, 1559
Kawaguchi, K., Kyutoku, K., Nakano, H., et al. 2015, PhRvD, 92, 024014
Kawaguchi, K., Shibata, M., & Tanaka, M. 2018, ApJL, 865, L21
Kawaguchi, K., Shibata, M., & Tanaka, M. 2020, ApJ, 889, 171
Kilpatrick, C. D., Foley, R. J., Kasen, D., et al. 2017, Sci, 358, 1583
Kiuchi, K., Sekiguchi, Y., Kyutoku, K., et al. 2015, PhRvD, 92, 064034
Korobkin, O., Rosswog, S., Arcones, A., & Winteler, C. 2012, MNRAS, 426, 1940
Kyutoku, K., Ioka, K., Okawa, H., Shibata, M., & Taniguchi, K. 2015, PhRvD, 92, 044028
Kyutoku, K., Ioka, K., & Shibata, M. 2013, PhRvD, 88, 041503
Lattimer, J. M., & Schramm, D. N. 1974, ApJ, 192, L145
Li, L.-X., & Paczyński, B. 1998, ApJL, 507, L59
Lippuner, J., & Roberts, L. F. 2015, ApJ, 815, 82
Lipunov, V. M., Gorbovskoy, E., Kornilov, V. G., et al. 2017, ApJL, 850, L1
Martin, D., Perego, A., Arcones, A., et al. 2015, ApJ, 813, 2
McCully, C., Hiramatsu, D., Howell, D. A., et al. 2017, ApJL, 848, L32
Metzger, B. D. 2017, LRR, 20, 3
Metzger, B. D., Martínez-Pinedo, G., Darbha, S., et al. 2010, MNRAS, 406, 2650
Metzger, B. D., Thompson, T. A., & Quataert, E. 2018, ApJ, 856, 101
Mooley, K. P., Deller, A. T., Gottlieb, O., et al. 2018, Natur, 561, 355
Nedora, V., Bernuzzi, S., Radice, D., et al. 2019, ApJL, 886, L30
Nicholl, M., Berger, E., Kasen, D., et al. 2017, ApJL, 848, L18
Perego, A., Radice, D., & Bernuzzi, S. 2017, ApJL, 850, L37
Perego, A., Rosswog, S., Cabezón, R. M., et al. 2014, MNRAS, 443, 3134
Pian, E., D'Avanzo, P., Benetti, S., et al. 2017, Natur, 551, 67
Radice, D., Galeazzi, F., Lippuner, J., et al. 2016, MNRAS, 460, 3255
Radice, D., Perego, A., Hotokezaka, K., et al. 2018a, ApJL, 869, L35
Radice, D., Perego, A., Hotokezaka, K., et al. 2018b, ApJ, 869, 130
Roberts, L. F., Kasen, D., Lee, W. H., & Ramirez-Ruiz, E. 2011, ApJL, 736, L21
Rosswog, S., Davies, M. B., Thielemann, F. K., & Piran, T. 2000, A&A, 360, 171
Rosswog, S., Liebendörfer, M., Thielemann, F. K., et al. 1999, A&A, 341, 499
Shappee, B. J., Simon, J. D., Drout, M. R., et al. 2017, Sci, 358, 1574
Siegel, D. M., & Metzger, B. D. 2017, PhRvL, 119, 231102
Siegel, D. M., & Metzger, B. D. 2018, ApJ, 858, 52
Smartt, S. J., Chen, T. W., Jerkstrand, A., et al. 2017, Natur, 551, 75
Soares-Santos, M., Holz, D. E., Annis, J., et al. 2017, ApJL, 848, L16
Symbalisty, E., & Schramm, D. N. 1982, ApL, 22, 143
Tanaka, M., Utsumi, Y., Mazzali, P. A., et al. 2017, PASJ, 69, 102
Tanvir, N. R., Levan, A. J., González-Fernández, C., et al. 2017, ApJL, 848, L27
Villar, V. A., Guillochon, J., Berger, E., et al. 2017, ApJL, 851, L21
Wanajo, S., Sekiguchi, Y., Nishimura, N., et al. 2014, ApJL, 789, L39
Wollaeger, R. T., Korobkin, O., Fontes, C. J., et al. 2018, MNRAS, 478, 3298
Wu, Y., & MacFadyen, A. 2019, ApJL, 880, L23